Emergence and coalescence of zonal jets: A quasilinear Rossby wave-mean flow interaction model

Daphné Lemasquerier *
School of Mathematics and Statistics, University of St. Andrews, St. Andrews, United Kingdom

(Received 11 July 2025; accepted 10 November 2025; published 8 December 2025)

Zonal jets are a fascinating natural example of how a rapidly rotating turbulent flow self-organizes at large scale in the presence of a β effect. Understanding the long-term, nonlinear equilibration of zonal jets and the feedback with the underlying turbulence and waves is still a challenge. Following a similar approach as in the Holton-Lindzen-Plumb model for mean flow reversals in stratified fluids, this study describes a novel, quasilinear semianalytical model to discuss the emergence and coalescence of zonal winds from the radiation of Rossby waves. This model emphasizes the role of Rossby waves in exchanging momentum with the zonal flow and the feedback of the zonal flow on the waves. It employs a Wentzel-Kramers-Brillouin expansion of the wave field to obtain an explicit expression for the Reynolds stress, leading to a closed mean flow equation. Two key feedback effects control the properties of the wave-driven zonal flow: the Doppler shift, leading to the emergence of critical latitudes, and the modification of the background β effect by the zonal flow curvature. Motivated by previous experimental observations, we integrate this quasilinear model in time with an increasing number of latitudes of wave radiation. We observe a transition between locally driven jets that remain individual and globally driven jets that coalesce and equilibrate at a new scale. In the weak wave damping limit, coalescence occurs when critical latitudes of neighboring jets overlap. This is the first purely zonal closure which self-consistently leads to an equilibrium flow with zonal jets separated by a Rhines scale. These results are further supported by quantitative comparison with experiments and nonlinear direct numerical simulations.

DOI: 10.1103/pqxy-x728

I. INTRODUCTION

Many planetary fluid layers exhibit persistent east-west currents called zonal jets [1], including Earth's oceans and atmosphere, the gas giants Jupiter and Saturn, and zonal jets are expected to exist in liquid cores [2] or in the atmospheres of brown dwarfs [3]. As reviewed in Galperin and Read [1], zonal jets are understood to arise from nonlinear interactions between eddies and waves ("fluctuations") and the zonal mean flow. This interaction has been investigated from the framework of potential vorticity mixing, Rossby wave-mean flow interactions, anisotropic turbulence, and modulational instabilities. Despite the extensive range of investigations, a general theoretical framework which could predict the width, spacing, and strength of zonal jets under a variety of forcing

*Contact author: d.lemasquerier@st-andrews.ac.uk

conditions is still missing. Furthermore, processes occurring during the long-term equilibration of jets, such as merging and spontaneous transitions between multistable states, remain outstanding issues.

The zonally averaged zonal wind, $\langle u \rangle$, arises from the Reynolds stress (or momentum flux), $\langle u'v' \rangle$, where u is the zonal velocity, v the meridional velocity, the brackets denote a zonal average, and primes represent departure from this average. The Reynolds stress is a nonlinear term representing velocity correlations between fluctuations that lead to the acceleration (or deceleration) of a zonal flow. Predicting the zonal flow profile that emerges from this nonlinear interaction under a variety of forcing conditions is an outstanding challenge. In general, it requires solving the equations that govern the dynamics of the fluctuations, which is computationally costly, and generally not analytically tractable.

Because the turbulent flow evolves on much smaller temporal scales and much shorter spatial scales than the mean flow, one way to (partly) alleviate this constraint is to use a quasilinear (QL) approximation. The QL approximation is a type of mean-field theory, where the nonlinear interaction between two waves that would produce a third wave is discarded [4]. The mean flow can be driven by the Reynolds stress produced by two waves (wave + wave $\rightarrow$ mean flow), and the mean flow has a feedback effect on waves (wave + mean flow $\rightarrow$ wave), but triad interactions (wave + wave $\rightarrow$ wave) responsible for energy cascades are discarded. QL models strongly rely on the assumption that the mean flow is dominant and fluctuations about the mean flow are small. In the limit of weak forcing and dissipation, Bouchet *et al.* [5] showed that the QL approximation is justified when there is a timescale separation between the mean flow and the eddies/waves. The advantage of QL models is that they drastically simplify a fully nonlinear system to make it analytically or numerically tractable, while retaining the essential features that control the dynamics of the mean flow. The QL approximation has been used in many fields of physics, and had its successes in the zonal jets problem [[4], and references therein]. Statistical QL models [6–11] have hence shown that zonal jets can form even in a framework where eddy-eddy interactions are ignored.

It is possible to go one step further in simplifying the system to avoid having to solve the wave equation altogether. The idea is to adopt a "turbulence closure" approach, and to derive an analytic expression for the Reynolds stress. If the Reynolds stresses are expressed as a function of the zonal flow itself and no wave component, then the mean flow equation becomes closed and can be evolved in time without having to solve the wave equation. The key challenge in this closure approach is that feedback effects between fluctuations and mean flow have to be properly modeled if one wants to capture the correct long-term equilibration and properties of the zonal flow.

Previous studies have investigated turbulence closures for coherent structures. Srinivasan and Young [12] predicted the Reynolds stress analytically for a stochastically forced, linearized β-plane flow with a background Couette flow, under the assumption of a spatially homogeneous steady solution. Jackman and Esler [13] developed the Srinivasan and Young [12] closure and showed that in general, it cannot be used as a purely zonal closure to predict the equilibrium zonal flow: Secondary nonzonal barotropic instabilities in eastward and westward jets have to be allowed to develop to correctly represent the momentum flux balance of the jets. Using a QL approximation, Woillez and Bouchet [14] predicted analytically the Reynolds stresses and zonal velocity profile in the limit of vanishing forcing and dissipation. They expressed the Reynolds stresses as a function of the mean flow shear and the energy injection rate, to close the mean flow equation. Their results are the first computations of Reynolds stresses and self-consistent velocity profiles from the turbulent dynamics. Local momentum flux closures of the same type have been proposed for the vortex condensate problem in isotropic two-dimensional turbulence [15–17] and successfully used to predict the radial velocity profile of the condensate. The Woillez and Bouchet [14] closure is however not as satisfactory for the zonal jets problem on a β plane: their closure and corresponding solution for the velocity profile diverges at the jet extrema (where the shear is zero), hence, it cannot predict the equilibrium jet flow without ad hoc regularizations of the eastward and westward jet extrema. As noted by Jackman and Esler [13], their closure is also independent of β and hence cannot lead to an equilibrium flow with jets separated by a Rhines scale. Here, we seek to use the QL approximation to provide a deterministic *nonlocal* analytical closure for the Reynolds stress. In particular, we propose a closure that can account for a forcing that is either *localized* in space (more relevant to the Earth's oceans and atmosphere) or *homogeneous* (more relevant to convective interiors and gas giant atmospheres). In the homogeneous case, due to feedback effects of the zonal flow on the Reynolds stress, our closure naturally leads to an equilibrium flow with jets separated by a Rhines scale.

The closure that we present in this paper is very much inspired by the Holton-Lindzen-Plumb model of the quasibiennial oscillation (QBO) [18–23]. This model explains the QBO by a QL model of gravity wave streaming in the stratosphere. Wave streaming is the process by which oscillating waves irreversibly force a mean flow when they dissipate, through the Reynolds stress divergence associated with the waves. Streaming was first discovered with acoustic waves damped by viscosity [24]. The Reynolds stresses due to the dissipation of the gravity wave (due for instance to viscosity, radiative damping or wave breaking) is calculated using a QL approximation, and used in the mean flow evolution equation to explain the emergence of oscillations.

In a similar fashion, a local emission of Rossby waves can generate a zonal flow, provided that the waves are dissipated at a different location than where they are generated. Because of the westward phase speed of Rossby waves, a prograde jet emerges in the wave-generating region while retrograde flows develop where Rossby waves dissipate. In this framework, if the forcing *and* the dissipation are homogeneous, no mean flow should emerge. This is the so-called nonacceleration theorem [25]. But this is true only if the retroaction of the mean flow on the waves propagation is neglected. Since the zonal flow modifies the local potential vorticity gradient (or background β effect), it makes the wave dissipation heterogeneous and jets effectively emerge even in the case of a homogeneous forcing [11].

Inspired by the Holton-Lindzen-Plumb model for mean flow reversals in a stratified fluid [26], we propose a novel semianalytical model for the emergence and long-term equilibration of barotropic zonal jets on a β plane. We provide a momentum flux closure by calculating the Reynolds stresses generated by the emission and attenuation of Rossby waves using a Wentzel-Kramers-Brillouin (WKB) approximation. This closure naturally incorporates two key feedback effects of the zonal flow on the waves, the Doppler shift and the modification of the background β effect. Using the analytical WKB momentum flux closure, we evolve numerically the mean flow in time. We predict a transition from a "localized" Rossby wave forcing situation, resulting in individually forced prograde jets, to a "homogeneous" or "global" forcing situation, where wave-driven jets interact, coalesce, and equilibrate at a new scale.

This modeling approach is further motivated by the experimental observation of Lemasquerier *et al.* [27,28]. In these turbulent zonal jets experiments, a transition was observed between a regime with six locally driven jets (correlated with the forcing rings) and two or three globally driven jets. Rossby wave dynamics was shown to be crucial to explain the transition and its bistability, however, the proposed theory could not explain the coalescence of the jets through the transition because the zonal velocity profile was assumed uniform. The present study reinstates an arbitrary zonal velocity profile and demonstrates that the retroaction of the mean flow on the wave field can account for the zonal jets coalescence observed experimentally.

The manuscript is organized as follows. In Sec. II, we derive the momentum flux closure for the zonal flow equation using a WKB expansion for the wave field and assuming a localized wave source. In Sec. III A, we evolve the mean flow in time using the closure for a single latitude of wave emission, and then in Sec. III B for multiple latitudes of wave emission. We compare the results of the QL model with nonlinear simulations (Sec. III C) and experiments (Sec. III D), and discuss relevance to planetary flows in Sec. IV A. We conclude in Sec. IV B.

II. QUASILINEAR MODEL

A. Zonal flow evolution equation

We consider a two-dimensional nondivergent barotropic flow with velocity components $\boldsymbol{u} = (u, v)$ in Cartesian coordinates (x, y), on an infinite β plane with planetary vorticity gradient β in the y direction. The y direction will be called "meridional" (north-south) hereafter, and the x-direction "zonal" (east-west). The vorticity of the fluid is $\nabla \times \boldsymbol{u} = \zeta \ \boldsymbol{e}_z$ with $\zeta = \partial_x v - \partial_y u$. We start by a Reynolds decomposition of the flow and decompose the velocity and vorticity into a zonal average plus fluctuations:

$$u = \langle u \rangle(y, t) + u'(y, x, t) = \langle u \rangle + u', \tag{1}$$

$$v = \langle v \rangle(y, t) + v'(y, x, t) = v', \tag{2}$$

$$\zeta = \langle \zeta \rangle(y, t) + \zeta'(y, x, t) = -\frac{\partial \langle u \rangle}{\partial y} + \zeta'. \tag{3}$$

Here, $\langle \cdot \rangle = \frac{1}{2\pi} \int_0^{2\pi} \cdot \, \mathrm{d}x$ is the zonal mean. In the following, we refer to $\langle u \rangle$ as the "zonal flow" and primed quantities are fluctuations (waves). The zonal average of the zonal component of the Navier-Stokes equation leads to the zonal flow evolution equation

$$\frac{\partial \langle u \rangle}{\partial t} = -\frac{\partial}{\partial y} \langle u' v' \rangle + \mathcal{D}[\langle u \rangle], \tag{4}$$

where $\mathcal{D}$ represents a dissipation operator. With this simple model, the only source term for the zonal flow is the first term on the right-hand-side: the divergence of the Reynolds stresses. Determining the Reynolds stress requires the solution of the wave equation. We will do so by using a WKB expansion of the wave field under a weak damping and long zonal wavelength limit. Readers familiar with this procedure are invited to jump to Eq. (16) which provides the corresponding expression for the Reynolds stress.

B. Rossby waves evolution equation

The goal is to derive an analytical expression of the Reynolds stresses divergence based on a WKB approximation of a damped wavefield emerging from a single latitude y_0. We start from the β-plane barotropic vorticity equation

$$\frac{\partial \zeta}{\partial t} + u \frac{\partial \zeta}{\partial x} + v \frac{\partial \zeta}{\partial y} + \beta v + r \zeta = 0, \tag{5}$$

where r is the wave damping rate. We rewrite this equation in terms of a stream function ψ ($u = -\partial_y \psi$, $v = \partial_x \psi$ and $\zeta = \nabla^2 \psi$):

$$\frac{\partial}{\partial t} \nabla^2 \psi + J(\psi, \nabla^2 \psi) + \beta \frac{\partial \psi}{\partial x} + r \nabla^2 \psi = 0, \tag{6}$$

where J is the Jacobian $J(g, h) = (\partial_x g)(\partial_y h) - (\partial_x h)(\partial_y g)$. Subtracting the zonally averaged equation, and linearizing about the background zonal flow by keeping only first order terms, we obtain the Rossby wave equation

$$\frac{\partial \nabla^2 \psi'}{\partial t} + \langle u \rangle(y) \frac{\partial \nabla^2 \psi'}{\partial x} + \underbrace{\left(\beta - \frac{\partial^2 \langle u \rangle}{\partial y^2} \right)}_{\beta^*} \frac{\partial \psi'}{\partial x} + r \nabla^2 \psi' = 0. \tag{7}$$

Note that here, we implicitly assume that the waves evolve on a shorter timescale compared to the slowly evolving zonal flow, i.e., the wavefield is computed in a quasistatic limit, assuming a stationary zonal flow $\langle u \rangle(y)$. Furthermore, wave-wave interactions are excluded from the linearized wave equation, hence they will not feed other waves. This is valid if nonlinear terms are small compared to the smallest linear term in the equation, which is the damping term under the weak damping limit that we will adopt in the following: $J(\psi', \nabla^2\psi')$ and $\langle J(\psi', \nabla^2\psi')\rangle \ll r\nabla^2\psi'$. However, wave-wave interactions will feed the zonal flow through the Reynolds stresses [Eq. (4)], making the model *quasi*linear.

The effective β effect, $\beta^* = \beta - \partial_y^2\langle u\rangle$, incorporates the modification of the β effect due to the retroaction of the zonal flow. For instance, β^* vanishes in a retrograde flow of curvature β, meaning that a retrograde zonal flow flattens the background potential vorticity (PV) gradient, i.e., decreases the effective β effect. In contrast, a prograde zonal flow (negative curvature) steepens the PV gradient, i.e., increases the effective β effect.

We consider plane wave solutions of zonal wave number k and zonal phase speed c:

$$\psi' = \tilde{\psi}(y)e^{ik(x-ct)} + \text{c.c.} \tag{8}$$

We consider a single Rossby wave with a westward phase speed, i.e., $c < 0$. Substituting into Eq. (7) leads to

$$\frac{d^2\tilde{\psi}}{dy^2} + l^2(y)\tilde{\psi} = 0, \tag{9}$$

where l is the modified meridional wave number which incorporates a damping (imaginary) term:

$$l^2 = \frac{\beta^*}{\langle u\rangle - c - ir/k} - k^2 = \frac{\beta^*}{\langle u\rangle - c}\left(1 + \left(\frac{r}{k(\langle u\rangle - c)}\right)^2\right)^{-1}\left(1 + \mathrm{i}\frac{r}{k(\langle u\rangle - c)}\right) - k^2. \tag{10}$$

Within the WKB approximation, we adopt a weak damping limit, $r \ll k(\langle u\rangle - c)$ and we additionally make the approximation $k \ll l$ (long zonal wavelength). The modified meridional wave number becomes

$$l^2 \approx \frac{\beta^*}{\langle u\rangle - c}\left(1 + \mathrm{i}\frac{r}{k(\langle u\rangle - c)}\right) = l_0(y)^2\left(1 + \mathrm{i}\frac{r}{k(\langle u\rangle - c)}\right). \tag{11}$$

In the following, we will use the attenuation distance Λ, which we define as the typical distance over which Rossby waves are damped and have deposited all their momentum. The meridional group velocity of Rossby waves is

$$c_g^y = \frac{2kl_0\beta^*}{\left(k^2 + l_0^2\right)^2} \approx \frac{2k\beta^*}{l_0^3} = \pm 2k\frac{(\langle u\rangle - c)^{3/2}}{(\beta^*)^{1/2}} \tag{12}$$

(see Ref. [25], Chap. 6), where the second approximation uses again $k \ll l_0$. Hence, the attenuation distance is given by

$$\Lambda = \frac{c_g^y(\langle u\rangle = 0)}{2r} = \frac{|k||c|^{3/2}}{r\beta^{1/2}}. \tag{13}$$

C. Momentum flux closure: Rossby waves streaming

1. WKB solution

Using a WKB expansion (see the full derivation provided in Appendix B), the solution to Eq. (9) is given by

$$\tilde{\psi}(y) = \tilde{\psi}_0\left(\frac{l_0(y)}{l_0(0)}\right)^{-1/2}\exp\left(\pm\mathrm{i}\int_y l\,dy'\right), \tag{14}$$

where $\tilde{\psi}_0$ is a constant (the wave amplitude) and l is given by Eq. (11). The Reynolds stress is given by

$$\langle u'v' \rangle = -ik\left(\tilde{\psi}\frac{d\overline{\tilde{\psi}}}{dy} - \overline{\tilde{\psi}}\frac{d\tilde{\psi}}{dy}\right), \tag{15}$$

where the overline denotes the complex conjugate.

Assuming that the wave amplitude $l_0(y)^{-1/2}$ varies slowly in the meridional direction compared with the meridional wavelength $(1/l_0)$, we neglect the meridional variations of $l_0(y)^{-1/2}$ when taking the y-derivative. This is justified if $dl_0/dy \ll l_0^2$, and we note that this condition breaks near critical latitudes ($\langle u \rangle = c$) where the wave amplitude varies rapidly. For a wave propagating northward and emitted from $y_0 = 0$, we then obtain

$$\langle u'v' \rangle^+ = -f_0 l_0^* \exp\left(-\int_0^y \frac{r(\beta^*)^{1/2}}{k(\langle u \rangle - c)^{3/2}} dy'\right) = -f_0 l_0^* \exp\left(-\frac{1}{\Lambda}\int_0^y \frac{\left[1-\beta^{-1}\partial_{y'}^2\langle u \rangle\right]^{1/2}}{[\langle u \rangle/|c|+1]^{3/2}} dy'\right), \tag{16}$$

where $^+$ denotes the northward wave ($y > 0$), and we recall that Λ is the attenuation distance [Eq. (13)]. f_0 is the Reynolds stress amplitude due to the wave radiation,

$$f_0 = \frac{2|k|\beta^{1/2}}{|c|^{1/2}}\tilde{\psi}_0^2, \tag{17}$$

and will be called the forcing amplitude hereafter. Finally, l_0^* is a multiplicative factor involving the zonal flow at the forcing latitude (see Appendix B):

$$l_0^* = \left[\frac{1-\beta^{-1}\partial_y^2\langle u \rangle}{\langle u \rangle/|c|+1}\right]_{y=0}^{1/2}. \tag{18}$$

Similarly, the momentum flux for a wave propagating southward ($y < 0$) is given by

$$\langle u'v' \rangle^- = +f_0 l_0^* \exp\left(+\frac{1}{\Lambda}\int_0^y \frac{\left[1-\beta^{-1}\partial_{y'}^2\langle u \rangle\right]^{1/2}}{[\langle u \rangle/|c|+1]^{3/2}} dy'\right). \tag{19}$$

The Reynolds stress is a decaying exponential over a typical distance which is the attenuation distance Λ. Hence, the Reynolds stresses divergence (alternatively called the streaming force) will be nonzero because of the attenuation of the wave. It is readily visible from Eq. (16) that the attenuation distance is however modified by the background zonal flow through two feedback effects. First, the zonal flow amplitude Doppler shifts the waves (term $\langle u \rangle/c + 1$). In the following, we call *critical latitudes* the y coordinates where $\langle u \rangle = c = -|c|$. Second, the zonal flow curvature modifies the planetary β effect (term $1 - \beta^{-1}\partial_y^2\langle u \rangle$), leading to so-called *turning latitudes* where the PV gradient vanishes, $\beta^* = \beta - \partial_y^2\langle u \rangle = 0$.

At the forcing latitude, $y_0 = 0$, the Reynolds stresses do a negative jump of $-2f_0 l_0^*$. The Reynolds stresses divergence would then be $-\partial_y\langle u'v' \rangle = 2f_0 l_0^*\delta(y)$ where δ is the Dirac distribution. This is not physical as it would correspond to an infinite prograde acceleration of the zonal flow at $y = 0$. Instead, we regularize this prograde acceleration over a Gaussian of finite width, Δy, such that its integral over the domain is $2f_0 l_0^*$, i.e., such that the total streaming force integrates to zero. Doing so, we introduce a new free parameter, the width of the forcing region Δy. The total Reynolds stress divergence is the sum of the contribution of the northward wave, the southward wave, and the regularization at the forcing latitude, and is given by

$$-\frac{\partial}{\partial y}\langle u'v'\rangle = -\frac{\partial}{\partial y}\langle u'v'\rangle^{+} - \frac{\partial}{\partial y}\langle u'v'\rangle^{-} + \frac{2f_0 l_0^*}{\sqrt{\pi}\Delta y}\exp\left(-\left(\frac{y}{\Delta y}\right)^2\right). \quad (20)$$

2. Nondimensionalization

We make the problem dimensionless by using the attenuation distance Λ as a length scale, the streaming time $\tau = |c|\Lambda/f_0$ as a timescale, where we recall that f_0 is the amplitude of the Reynolds stresses (m^2s^{-2}), and $f_0\tau/\Lambda = |c|$ as the velocity scale. In the following, we denote dimensionless variables with uppercase letters:

$$x \to X\Lambda, \quad y \to Y\Lambda, \quad t \to T\tau, \quad (21)$$

$$(\langle u\rangle, u', v') \to (\langle U\rangle, U', V')|c|, \quad \psi \to \Psi\Lambda|c|. \quad (22)$$

We define the dimensionless wave damping parameter

$$\gamma = \left(\frac{kc}{r}\right)^2 = \frac{\beta\Lambda^2}{|c|}. \quad (23)$$

In the weak damping limit relevant for the WKB expansion, $\gamma \gg 1$ and $\gamma^{-1/2}$ is used as a small parameter when expanding the variables (Appendix B).

For northward and southward waves emitted from the latitude $Y = Y_0$, the dimensionless WKB closure for the Reynolds stress divergence yields

$$-\frac{\partial}{\partial Y}\langle U'V'\rangle = \frac{2M_0(Y_0)}{\sqrt{\pi}\Delta Y}\exp\left(-\left(\frac{Y-Y_0}{\Delta Y}\right)^2\right) - \begin{cases} G(U)M_0(Y_0)\exp\left(-\int_{Y_0}^{Y} G(U(Y'))dY'\right) & \text{for } Y > Y_0 \\ G(U)M_0(Y_0)\exp\left(\int_{Y_0}^{Y} G(U(Y'))dY'\right) & \text{for } Y < Y_0 \end{cases} \quad (24)$$

where the integrand represents the dimensionless inverse of an attenuation distance

$$G(U;\gamma) = \frac{\left(1-\gamma^{-1}\frac{\partial^2\langle U\rangle}{\partial Y^2}\right)^{1/2}}{(\langle U\rangle + 1)^{3/2}}, \quad (25)$$

and

$$M_0(Y_0) = \left(\frac{1-\gamma^{-1}\partial_Y^2\langle U\rangle_{Y=Y_0}}{\langle U\rangle_{Y=Y_0}+1}\right)^{1/2} \quad (26)$$

(see Appendix B). In dimensionless quantities, the case $\langle U\rangle = -1$ corresponds to a critical latitude and a vanishing PV gradient corresponds to $1-\gamma^{-1}\partial_Y^2\langle U\rangle \to 0$.

3. No background zonal flow

To help build some intuition, we first examine the case with no background zonal flow, $\langle U\rangle = 0$, and consider waves radiated from $Y = 0$. Note that this case does not require a WKB expansion for the wave solution, and the interested reader is referred to Appendix A for a more physically insightful derivation of the solution.

In the absence of zonal flow, the solution at leading order in $\gamma^{-1/2}$ is a damped meridional oscillation:

$$\tilde{\Psi} = \tilde{\Psi}_0 \exp\left(i\gamma^{1/2}Y - Y/2\right). \quad (27)$$

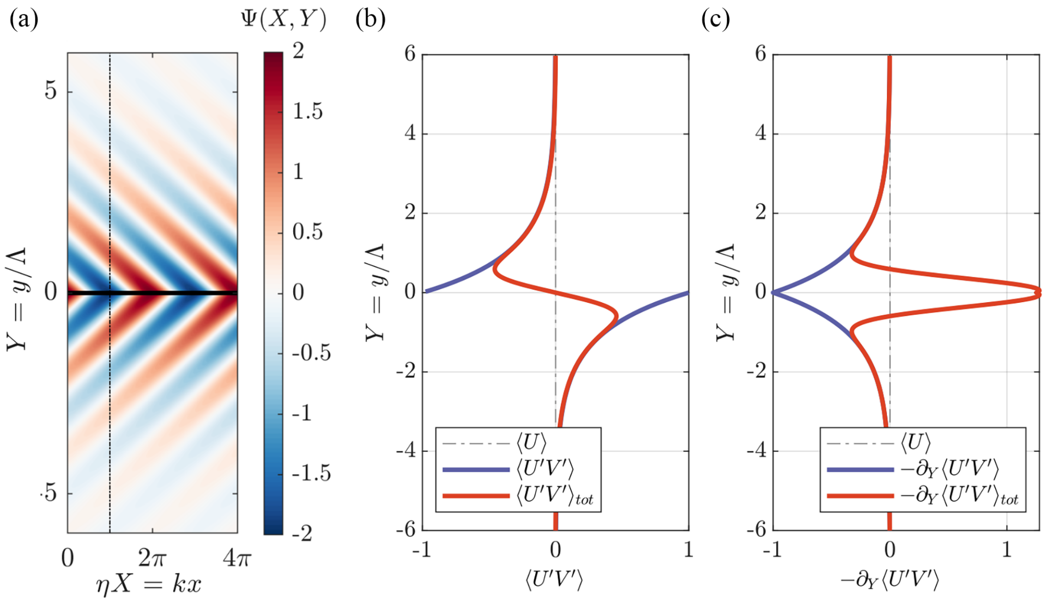

FIG. 1. Illustration of momentum flux due to Rossby waves radiated from a single latitude $Y = 0$ in the absence of background zonal flow ($\langle U \rangle = 0$). Plotted quantities are made dimensionless using the attenuation distance Λ and the phase speed $|c|$ (see Sec. II C 2). (a) Wave field (stream function). (b) Reynolds stresses. (c) Reynolds stresses divergence. For the purpose of illustration, $\eta = k\Lambda = 0.01$ and $\gamma = (kc/r)^2 = 10$. In panels (b) and (c), the jump of Reynolds stresses at the forcing location is regularized over a forcing width $\Delta Y = \Delta y/\Lambda = 0.5$ (red curves).

Figure 1(a) shows the corresponding wave field, $\Psi' = \tilde{\Psi}(Y)e^{i\eta X} + \text{c.c.}$, where $\eta = k\Lambda$ is the dimensionless zonal wave number.

Figure 1(b) shows the corresponding Reynolds stress profile, in blue without the regularization of the jump at the forcing latitude, and in red with the regularization. The dimensionless Reynolds stresses are simply decaying exponentials of opposite sign with an e-folding distance of 1 in dimensionless quantities. For the northward wave and southward wave, respectively,

$$\langle U'V' \rangle^+(Y) = -\exp(-Y) \text{ for } Y > 0, \tag{28}$$

$$\langle U'V' \rangle^-(Y) = \exp(+Y) \text{ for } Y < 0. \tag{29}$$

For a wave propagating northward (positive meridional group velocity), the Reynolds stresses are negative, whereas for a southward propagating wave, the Reynolds stresses are positive.

The divergence of the Reynolds stresses $[-\partial_Y \langle U'V' \rangle = -\exp(-|Y|)]$, alternatively called the streaming force, is negative for both the northward and southward wave, as represented in Fig. 1(c). Physically, the negative Reynolds stresses divergence arises from the westward phase speed of Rossby waves, which deposit westward momentum when they dissipate. Hence, a retrograde flow is accelerated away from the forcing region. Adding the regularization over the forcing region of width ΔY, the total streaming force is given by

$$-\frac{\partial \langle U'V' \rangle}{\partial Y} = -\exp(-|Y|) + \frac{2}{\sqrt{\pi}\,\Delta Y} \exp\left(-\left(\frac{Y}{\Delta Y}\right)^2\right) \tag{30}$$

and is represented by the red curve in Fig. 1(c). Overall, a localized Rossby wave radiation in the absence of background zonal flow will accelerate a prograde jet in the forcing region, and a retrograde flow on the flanks of the jet.

4. Feedback of the zonal flow

Let us know consider the background zonal flow $\langle U\rangle(Y)$ to be an arbitrary function of latitude. The attenuation distance [Eq. (25)] is affected by the zonal flow amplitude and curvature. Therefore, we expect a strong feedback of the zonal flow on the streaming force.

Let us first focus on the feedback of the zonal flow amplitude, illustrated in Figs. 2(a)–2(c). Equations (16) and (25) show that the modified attenuation distance decreases when the zonal flow speed is negative (retrograde) and goes to zero when the zonal flow speed approaches the wave phase speed ($\langle u\rangle \to c = -|c|$, i.e., $\langle U\rangle \to -1$). This represents the fact that the wave is more attenuated in a retrograde flow and less attenuated in a prograde flow [Fig. 2(a)], and has been fully dissipated when it reaches a critical latitude. Figure 2(c) shows the corresponding streaming force: the wave deposits all of its momentum in the region between the forcing latitude and the critical latitude, and the streaming force is null beyond the critical latitude.

At a critical latitude, the meridional wave number l_0 goes to infinity [Eq. (11)], hence the wave amplitude ($\propto l_0^{-1/2}$) goes to zero, and the wave energy ($\propto (k^2 + l_0^2)/l_0$ [25]) goes to infinity. Strictly speaking, this means that both the quasilinear and weak damping approximations break down, and nonlinear effects should become important in some vicinity of the critical latitude. A detailed treatment of processes within critical layers is beyond the scope of our study, but let us mention a few points. Closed contours known as "cat's eyes" form in the critical layer, and eventually overturn and break, and the wave is either absorbed or reflected [29–32]. The wave hence does not carry momentum beyond the critical latitude. While the WKB model cannot capture wave breaking, by construction, the wave deposits all of its momentum before it reaches a critical latitude, which is not a too bad representation of what should be happening. We note that this is similar to what happens at critical lines in the Holton-Lindzen-Plumb model for the QBO [26]. Another subtle point is that if the wave is not dissipated before it reaches the critical latitude, the nonlinear dynamics occurring in the critical layer could itself locally accelerate a mean flow [32]. This will depend on the degree of absorption versus reflection of the incident wave, and to the best of our knowledge, this is still subject of debate and depends on details of the incident wave [31].

We now discuss the feedback of the zonal flow curvature, illustrated in Figs. 2(d)–2(f). When the zonal flow curvature approaches β, the effective β effect goes to zero, or said differently, the PV gradient vanishes. This corresponds to $\beta^* = \beta - \partial_y^2\langle u\rangle \to 0$, or $1 - \gamma^{-1}\partial_Y^2\langle U\rangle \to 0$ in dimensionless quantities. At these turning latitudes, $l \to 0$, i.e., the meridional wavelength diverges. Hence, even though the amplitude and the energy of the wave diverges, it should not break, highlighting the difference with critical latitudes [25]. The Reynolds stress and streaming force in this case is illustrated in Figs. 2(e) and 2(f). Because the integrand goes to zero, the waves are not attenuated. The Reynolds stresses are constant over the region where $\partial_Y^2\langle U\rangle = \gamma$, so the Reynolds stresses divergence vanishes and there is no streaming acceleration of the zonal flow. This means that as a retrograde flow develops, it reduces the effective β, hence reduces the streaming force. This is a negative feedback effect which, by construction, prevents the acceleration of a retrograde flow with a curvature exceeding β.

D. Closed zonal flow equation

Having derived a momentum flux closure, it can be substituted in the zonal flow evolution equation:

$$\frac{\partial\langle u\rangle}{\partial t} = -\frac{\partial}{\partial y}\langle u'v'\rangle + \nu\frac{\partial^2\langle u\rangle}{\partial y^2}. \tag{31}$$

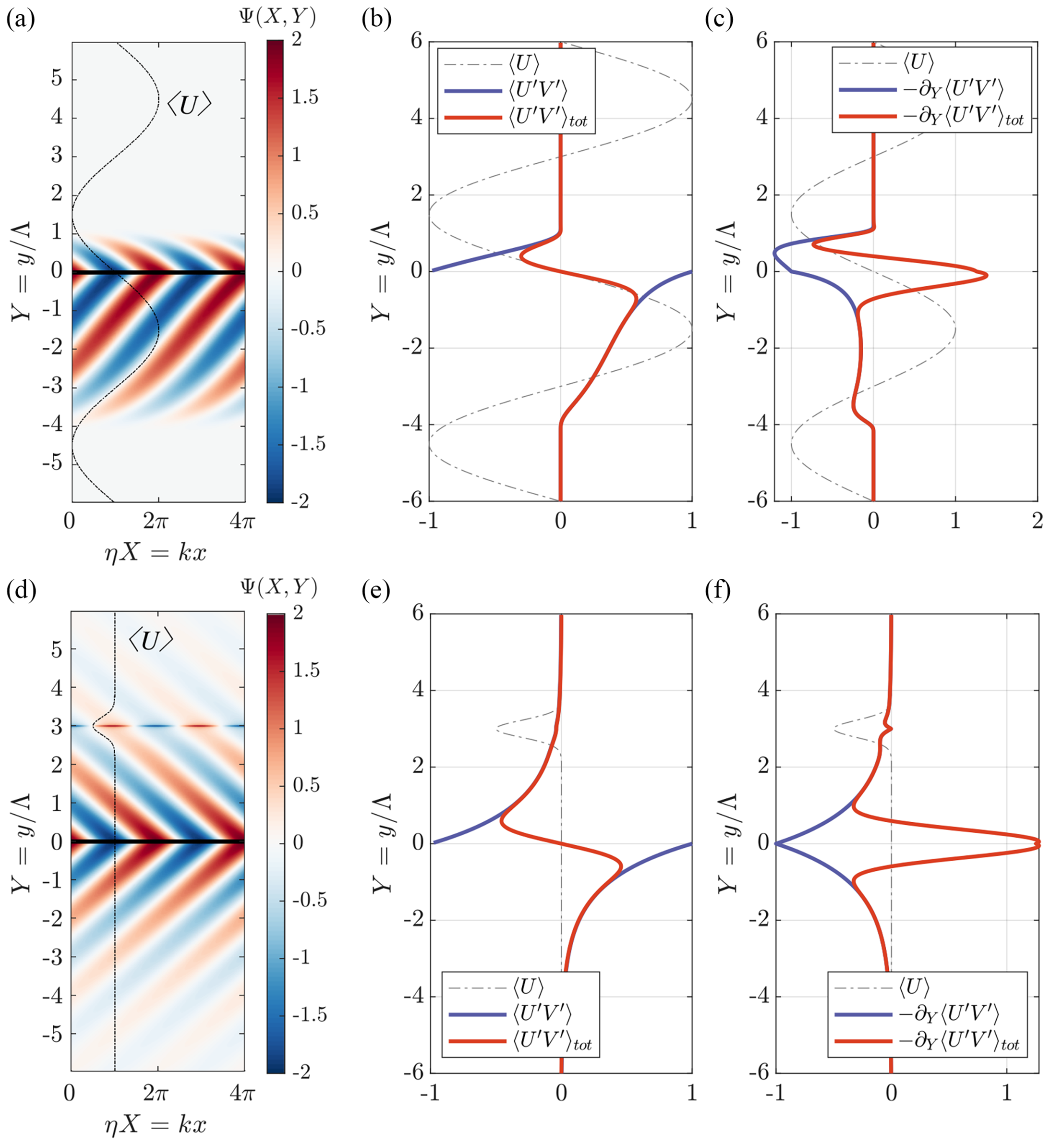

FIG. 2. Illustration of the feedback effects of a nonzero zonal flow $\langle U\rangle(Y)$ on the streaming force due to Rossby waves radiated at $Y = 0$. The dimensionless version of the Reynolds stresses is provided in Eqs. (24) and (25). For the purpose of illustration, $\eta = 0.01$, $\gamma = 10$, $\Delta Y = 0.5$. The jump of Reynolds stresses at the forcing latitude is regularized over the forcing distance ΔY (red curves). The dashed curves represent the background zonal flow. (a)–(c) Case with two critical latitudes ($\langle u\rangle \to c$, or $\langle U\rangle \to -1$ in dimensionless quantities). (d)–(f) Case with vanishing potential vorticity gradient at $Y = 3$, i.e., vanishing effective β effect ($\partial_y^2\langle u\rangle \to \beta$, or $1 - \gamma^{-1}\partial_Y^2\langle U\rangle \to 0$ in dimensionless quantities).

Here, we consider only viscous dissipation, and ν should be considered as molecular kinematic viscosity in a rotating tank experiment, but turbulent viscosity on a gas giant. Using the dimensionless variables of Sec. II C 2, the dimensionless version of Eq. (31) is given by

$$\frac{\partial\langle U\rangle}{\partial T} = -\frac{\partial}{\partial Y}\langle U'V'\rangle + \frac{1}{\mathrm{Re}}\frac{\partial^2\langle U\rangle}{\partial Y^2}, \tag{32}$$

where the Reynolds number compares the magnitude of the wave forcing relative to viscous dissipation:

$$\mathrm{Re} = \frac{f_0 \Lambda}{\nu |c|}. \tag{33}$$

The dimensionless WKB closure for the Reynolds stresses divergence is given by Eq. (24). Hence, Eq. (32) is a one-dimensional integrodifferential equation.

For a single latitude of emission Y_0, the free parameters of the problem are the forcing width (ΔY), the wave damping parameter (γ) and the forcing Reynolds number (Re). Equation (32) is advanced in time using the Runge-Kutta 4 scheme, spatial derivatives are calculated using fourth order accuracy centered finite differences, and the integral is evaluated using the Simpson rule. Periodic boundary conditions are imposed. The initial condition is a flow at rest with a noise of amplitude 1×10^{-3}. To ensure that the waves necessarily "break" right after critical latitudes located at $Y = Y_c$, we set the streaming force to zero at latitudes greater than a critical latitude. For the northward wave,

$$-\partial_Y \langle U'V' \rangle = 0, \ \forall\, Y \geqslant Y_c, \tag{34}$$

and we proceed similarly for the southward wave. The effective β is also set to zero whenever the zonal flow curvature exceeds β, i.e., whenever $\partial_Y^2 \langle U \rangle \geqslant \gamma$.

III. RESULTS

A. Single latitude of wave emission: The streaming process

1. Single jet emergence and feedback

We integrate Eq. (32) starting from rest for a single latitude of wave emission, located at $Y = 0$, with $\gamma = 100$. The evolution of the zonal flow profile is represented in Figs. 3 and 4 for three different values of the forcing Reynolds, $\mathrm{Re} = 10^{0.5}, 10^{1}, 10^{1.5}$, to illustrate different degrees of feedback effects from the zonal flow. In the three cases, a prograde jet emerges at $Y = 0$, flanked by retrograde flows. For $\mathrm{Re} = 10^{0.5}$, the zonal jet is weak, and its feedback on the wave streaming is limited [Figs. 3(a) and 4(a)]: no critical latitudes are formed ($\langle U \rangle \neq -1$) and the effective β is very close to the planetary β effect ($1 - \gamma^{-1}\partial_y^2 \langle U \rangle \approx 1$). For a higher Reynolds, $\mathrm{Re} = 10^1$, the amplitude of the zonal jet is higher and the retrograde flow reaches a value close to -1 [Figs. 3(b) and 4(b)]. Simultaneously, the curvature of the retrograde flanks becomes significant enough to modify the background β effect: the effective β effect is higher in the prograde jet, and lower in the retrograde flanks. The negative streaming force is confined between the forcing latitude, $Y = 0$, and $Y \approx \pm 1$ where critical latitudes almost form ($\langle U \rangle$ approaches -1). For an even higher Reynolds, $\mathrm{Re} = 10^{1.5}$, both critical latitudes and regions of vanishing effective β effect are formed, efficiently confining the streaming force in latitude [Figs. 3(c) and 4(c)]. Beyond the critical latitudes, the streaming force goes to zero, and the retrograde flow propagates in latitude due to slow viscous diffusion only.

We observe that for large $\gamma \gtrsim 5$, regions where $\beta^* = 0$ and critical latitudes appear almost simultaneously, and at the same location [Fig. 3(c)]. This is not surprising since as the retrograde flow forms, the curvature increases. In cases at low γ however, the two feedback effects are more sequential. In our model, the curvature of the zonal flow cannot exceed γ. At low γ, the maximum authorized curvature is small and is rapidly reached. While maintaining this fixed maximum curvature, the retrograde jets have the time to expand meridionally outward until a minimum value of $\langle U \rangle = -1$ is reached and the critical latitude prevents further meridional expansion. In this case, the region where $\beta^* = 0$ is meridionally extended, but still overlaps the critical latitude.

2. Parameter survey

The Reynolds number Re was varied logarithmically from $10^{-0.5}$ to 10^3 in steps of 0.5 in the exponent, and γ was varied from $10^{0.5}$ to 10^3. Figure 5 shows the zonal flow profile, amplitude

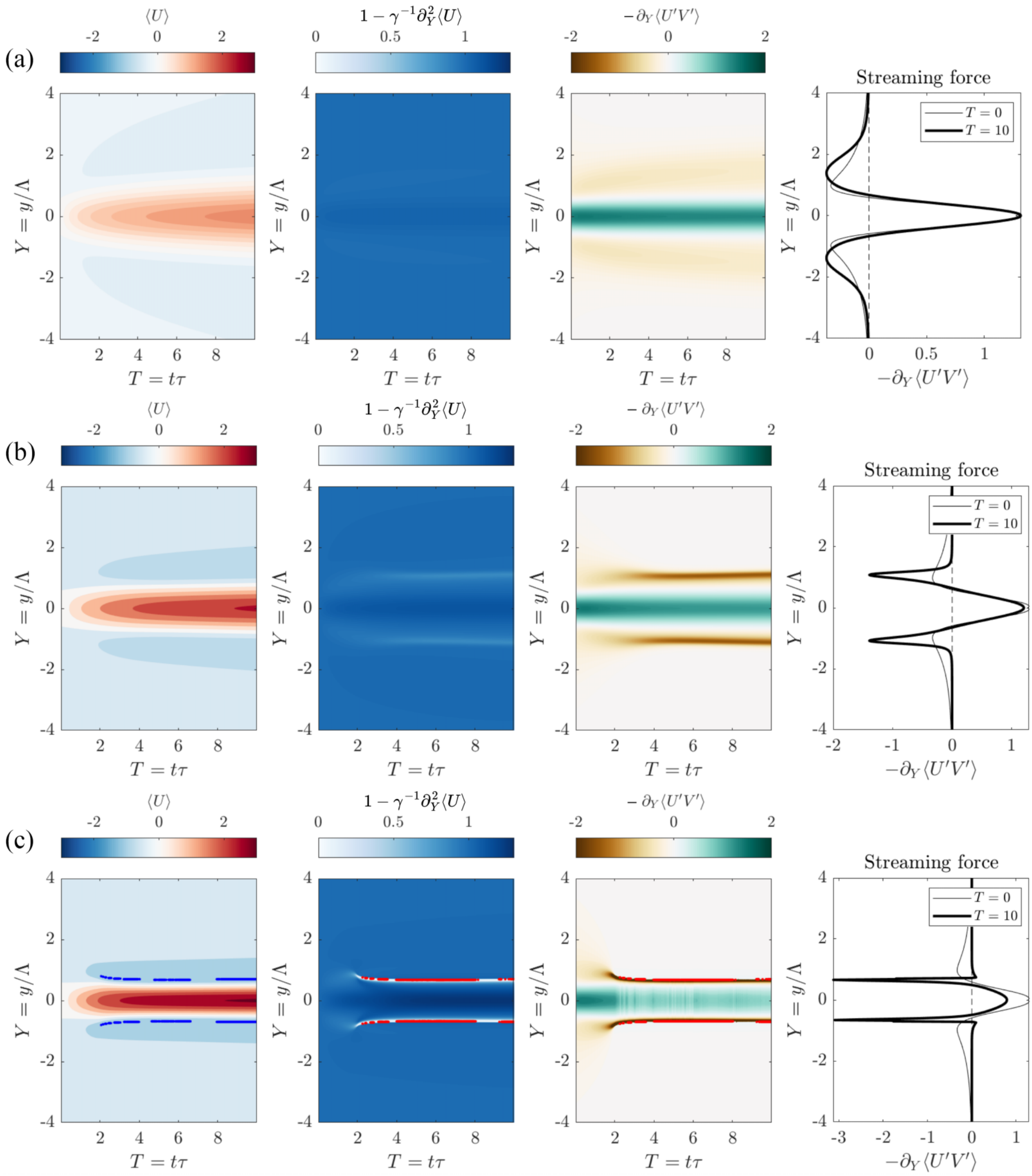

FIG. 3. Emergence of a zonal jet for a single latitude of wave emission at $Y = 0$ ($\gamma = 100$, $\Delta Y = 0.5$). The four columns show the zonal flow profile, the effective β effect, the streaming force, and the streaming force profiles at the beginning (thin line) and at the end (thick line) of the integration. (a) $\mathrm{Re} = 10^{0.5}$, (b) $\mathrm{Re} = 10^{1}$, (c) $\mathrm{Re} = 10^{1.5}$. On the zonal flow space-time diagram, the blue line represent locations where critical latitudes form, $\langle U\rangle < -0.99$. The red lines represent locations where the effective β vanishes, $1 - \gamma^{-1}\partial_Y^2\langle U\rangle < 0.01$.

(U_{jet}) and width (ΔY_{jet}). The prograde jet width is measured as the distance between the two zeros of the zonal flow profile, and the amplitude is taken as the maximum zonal flow speed. At small Re, the zonal flow amplitude is limited by diffusion, since the retrograde flanks have not formed critical latitudes [Fig. 5(a), crosses in Fig. 5(b)], hence, $U_{\mathrm{jet}} \sim \mathrm{Re}$ [dashed line in Fig. 5(b)]. When Re increases, the retrograde flow gets closer to -1, and eventually critical latitudes form on the retrograde flanks [full circles in Fig. 5(b)]. The formation of critical latitudes prevents further growth

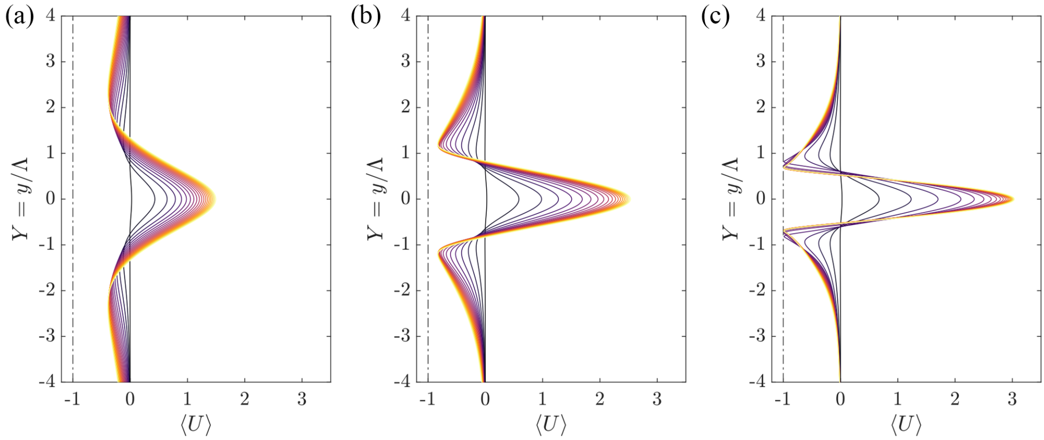

FIG. 4. Zonal flow profiles corresponding to Fig. 3: (a) $\mathrm{Re} = 10^{0.5}$, (b) $\mathrm{Re} = 10^1$, (c) $\mathrm{Re} = 10^{1.5}$. The color scale (purple to yellow) represents 20 linearly spaced times from $T = 0$ to $T = 10$. The dashed line represents $\langle U \rangle = -1$.

of the jet, hence the plateau in U_{jet} for $\mathrm{Re} > 10$. The prograde jet width, represented in Fig. 5(c), transitions from a large diffusive scale, to the scale of the forcing width, in the limit $\gamma \gg 1$ and $\mathrm{Re} \gg 1$. For intermediate values of γ, when critical latitudes form (full circles), the jet width saturates at a value dependent on γ that we explain later.

Figures 5(d)–5(f) show similar quantities for a sweep in γ at fixed Re. Figure 5(f) shows that at low Re, when no critical latitudes emerge (crosses), the jet width is almost independent of γ: because of strong viscous dissipation compared to the wave forcing, the zonal flow amplitude and curvature are small and feedback effects are negligible ($1 + \langle U \rangle \approx 1$ and $1 - \gamma^{-1}\partial_Y^2\langle U \rangle \approx 1$). As Re is increased, feedback effects become stronger, and in particular, critical latitudes are formed in the retrograde flanks [Fig. 5(d) and full circles in Fig. 5(f)]. In this case, the jet width decreases with γ. This is because γ is effectively the maximum curvature of retrograde flanks ($\partial_Y^2\langle U \rangle \leqslant \gamma$) otherwise the effective β would become negative. When γ increases, the authorized curvature of retrograde flows is higher, explaining why the jet width decreases, as visible in Fig. 5(d).

To quantify this, let us consider the configuration sketched in Fig. 6(a). Let us center a critical latitude at $Y = 0$ ($\langle U \rangle(0) = -1$), and assume that this is a local zonal flow minimum, $\partial_Y\langle U \rangle(0) = 0$, and that the curvature of the retrograde flank is $\partial_Y^2\langle U \rangle = \gamma$. This leads to $\langle U \rangle(Y) = \gamma Y^2/2 - 1$. To find the position of the prograde peak, we denote D the distance between the prograde peak and the critical latitude. By conservation of angular momentum, we impose $\int_0^D \langle U \rangle \mathrm{d}Y = 0$, from which we obtain $D = \sqrt{6/\gamma}$. With this zonal flow profile, the velocity at the prograde peak is $U_{\max} = 2$. The width of the jet, taken to be twice the distance between the prograde peak and the first zero crossing is predicted to be $\Delta Y_{\text{jet}} = 2(\sqrt{6} - \sqrt{2})\gamma^{-1/2} \approx 2.07\gamma^{-1/2}$.

This prediction is fully supported by Fig. 5 which shows that for $\mathrm{Re} \gtrsim 100$, the jet width scales as $\gamma^{-1/2}$ [full lines in Fig. 5(c), dashed line in Fig. 5(f)]. When critical latitudes are formed, the width of the prograde jet is hence set by the maximum curvature of the retrograde flank. For sufficiently large γ, this “curvature-controlled” width becomes smaller than the imposed forcing width, ΔY, hence the jet width converges to ΔY in the limit $\gamma \gg 1$ and $\mathrm{Re} \gg 1$ [Fig. 5(c)].

B. Multiple latitudes of wave emission

To investigate the interaction of multiple wave-driven jets, we now impose n_f equidistant forcing latitudes in the periodic domain of size $L = 12$. The dimensionless initial jet spacing is denoted

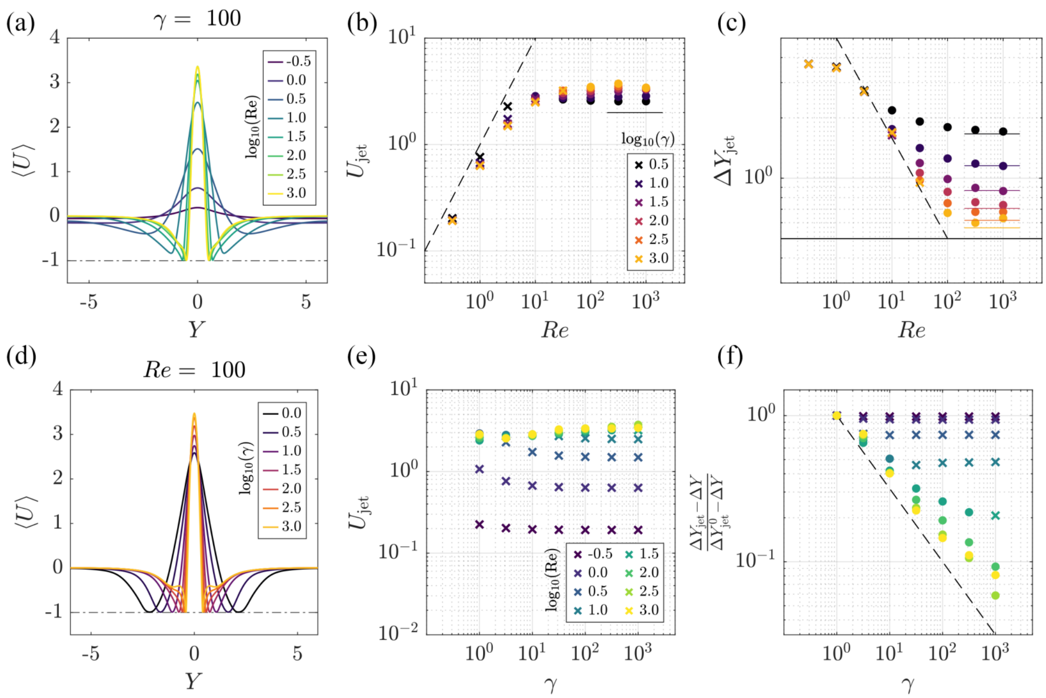

FIG. 5. Zonal flow properties for Re varied logarithmically from $10^{-0.5}$ to 10^3 and γ varied from 10^0 to 10^3. Cases where critical latitudes form are denoted with full circles, in contrast with crosses. The forcing width is fixed at $\Delta Y = 0.5$. (a), (d) Zonal flow profile. (b), (e) Zonal flow amplitude. In panel (b), the dashed line is $\propto$ Re. (c), (f) Zonal jet width. In panel (c) the horizontal colored lines indicate the predicted jet width, $2(\sqrt{6}-\sqrt{2})\gamma^{-1/2}$. The dashed line is $\mathrm{Re}^{-1/2}$. The horizontal black line is the forcing width ΔY. In panel (f) $\Delta Y^0_{\mathrm{jet}}$ is the jet width for $\gamma = 1$. The dashed line is $\gamma^{-1/2}$.

$D_{\mathrm{jet,i}} = L/n_f$. We hence integrate the equation

$$\frac{\partial \langle U\rangle}{\partial T} = -\frac{\partial}{\partial Y}\sum_{i=1}^{n_f}\langle U'V'\rangle_i + \frac{1}{\mathrm{Re}}\frac{\partial^2\langle U\rangle}{\partial Y^2}, \tag{35}$$

where $\langle U'V'\rangle_i$ are the Reynolds stresses due to a northward and a southward wave emitted at $Y = Y_i$. Our working hypothesis is that interactions between individually forced jets will occur when forcing latitudes are sufficiently close to each other.

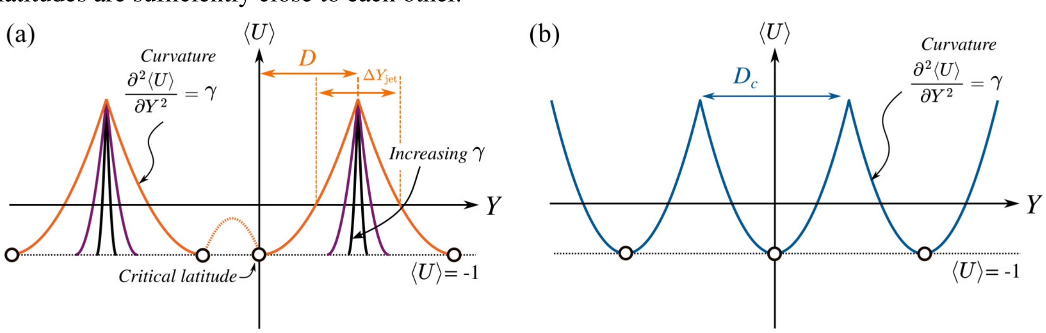

FIG. 6. Model of the zonal flow profile in the presence of critical latitudes. (a) Shielded jets. $D \sim \gamma^{-1/2}$ is the distance between the prograde jet peak and the critical latitude in either of the retrograde flanks. (b) $D_c = 2D$ is the jet spacing at which the critical latitudes of two adjacent jets coincide.

1. Transition between locally forced and globally forced jets

If we consider a case where critical latitudes form, one can assume that since the streaming force vanishes beyong critical latitudes, then neighboring jets will be able to interact only when their respective critical latitudes overlap. We have estimated that the distance between the jet peak and the critical latitude is $D \sim \sqrt{6}\gamma^{-1/2}$. Therefore, the critical jet spacing for which the critical latitudes of two neighboring jets overlap is $D_c = 2D = 2\sqrt{6}\gamma^{-1/2}$ [Fig. 6(b)]. This critical jet spacing estimate completely ignores the finite forcing width, ΔY. If $\gamma \gg 1$, then D_c can be smaller than the forcing width, in which case we expect the forcing width to become the limiting distance at which jets start to interact. We hence predict $D_c = \max(2\sqrt{6}\gamma^{-1/2}, a\Delta Y)$, where a is a prefactor to be determined.

Figure 7 shows two cases for $\gamma = 10$, $\mathrm{Re} = 100$, and $\Delta Y = 0.5$. With these parameters, the predicted critical jet spacing is $D_c = 1.55$. Figure 7(a) shows the case $D_{\mathrm{jet,i}} = 2.40$ ($n_f = 5$ forcing latitudes). In this first scenario ($D_{\mathrm{jet,i}} > D_c$) five independent prograde jets are formed, the jets are shielded by their respective critical latitudes, and the regions where the effective β vanishes are well separated from each other. Figure 7(b) shows the case $D_{\mathrm{jet,i}} = 1.33$ ($n_f = 9$ forcing latitudes). In this second scenario ($D_{\mathrm{jet,i}} < D_c$), nine prograde jets initially develop. Because the forcing latitudes are close enough, the curvature of the retrograde jets reaches β before critical latitudes are formed [see the dashed purple curves in Fig. 7(b)]. A transition occurs during which six jets out of nine vanish and the system reaches a new equilibrium made of three shielded prograde jets of higher amplitude.

A complete sweep in initial jet spacing for $\gamma = 10$, with $D_{\mathrm{jet,i}}$ decreasing from 4 to 0.52, is represented in Fig. 8. From $n_f = 3$ to 7, the critical latitudes of each jet get closer to each other, until being almost superposed at $n_f = 7$. The transition between locally and globally driven jets occurs between $n_f = 7$ and $n_f = 8$, i.e., for $D_{\mathrm{jet,i}} \in]1.50, 1.71[$, consistent with a critical spacing of $D_c = 1.55$. The number of jets in the new equilibrium after the transition varies between three to five. Interestingly, the structure of the jets after a transition is very close to the structure of the jets emerging in the case of locally forced, individual jets with the corresponding number of forcing latitudes (Fig. 9).

2. Regime diagrams

We performed similar sweeps for different values of Re and γ, and represent the results on the regime diagrams of Fig. 10. Figure 10(a) shows the evolution of the critical jet spacing with γ for a fixed $\mathrm{Re} = 100$. The criterion $D_c \approx 2\sqrt{6}\gamma^{-1/2}$ (dashed blue line) predicts very well the transition threshold for $\gamma \in [1, 10]$, suggesting that the overlapping of critical latitudes of neighboring jets is indeed the process which triggers coalescence. For $\gamma > 10$, the distance at which critical latitudes would overlap becomes close to the distance at which the width of the forcing region starts to overlap ($2\Delta Y = 1$, red line). The critical distance then becomes independent of γ, and here we obtain $D_c \approx 1.15 = 2.3\Delta Y$. This regime diagram is therefore consistent with the criterion $D_c = \max(2\sqrt{6}\gamma^{-1/2}, a\Delta Y)$, with $a \approx 2.3$.

Figures 10(c) and 10(d) show the evolution of the average jet width for increasing n_f, at fixed $\gamma = 10$ and $10^{1.5}$ corresponding to the vertical lines in Fig. 10(a). Figure 10(c) ($\gamma = 10$) shows a case which is curvature controlled. The jet width obtained when the curvature is β and minimum velocity is c (dashed blue line) is larger than the forcing width (red line), i.e., $2(\sqrt{6} - \sqrt{2})\gamma^{-1/2} > \Delta Y$. The coalescence hence occurs when two critical latitudes overlap. Figure 10(d) ($\gamma = 10^{1.5}$) shows the opposite case where the minimum jet width is smaller than the width of the forcing region, hence coalescence happens due to overlapping forcing regions, not overlapping critical latitudes. Figure 16 in the Appendix shows the coalescence process in this second scenario where it is controlled by the forcing width.

Figure 10(b) shows the evolution of the critical jet spacing with Re for a fixed $\gamma = 2.2$. This small value of γ was chosen to match experimental parameters, as discussed later in Sec. III D. For low Re, as Re increases (the wave forcing increases), the critical jet spacing increases. This can again be explained by a curvature-controlled criterion. At low Re, the individually forced jets are in

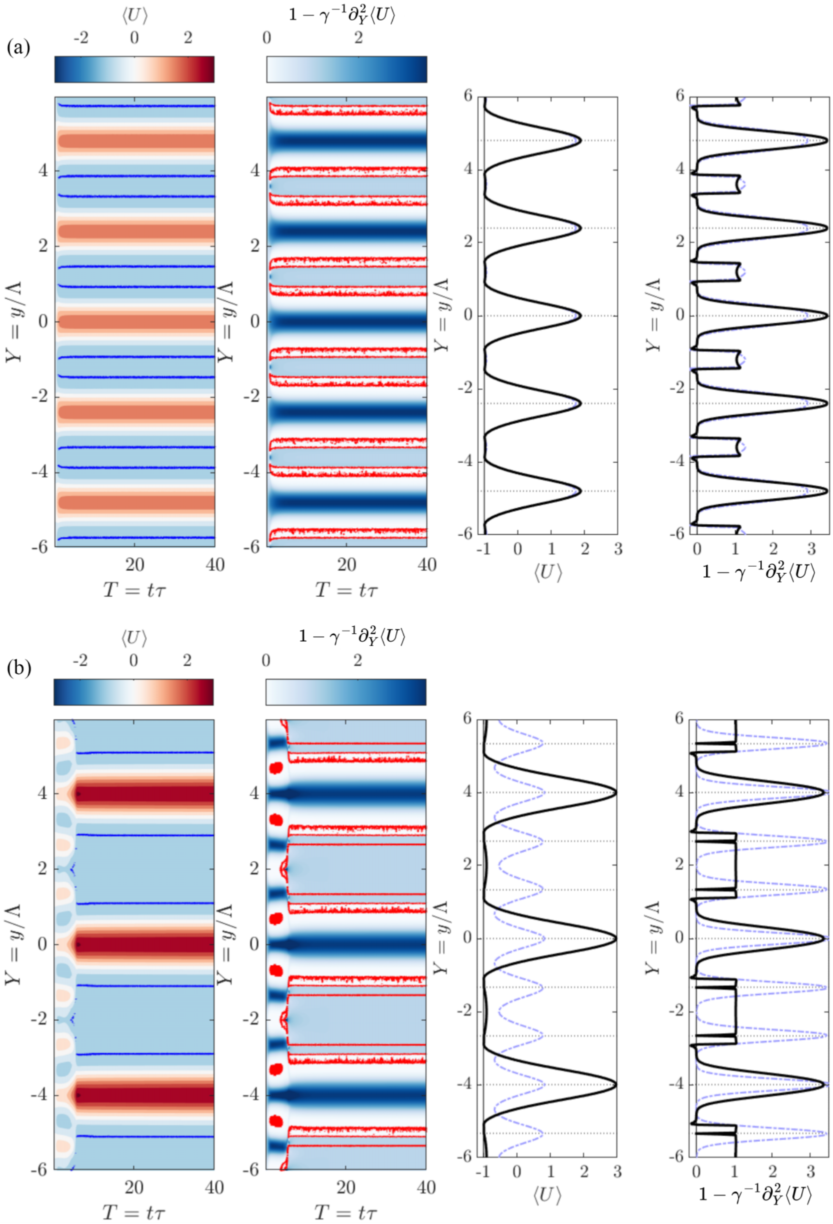

FIG. 7. Two regimes of wave-driven jets forced at multiple latitudes with $\gamma = 10$, Re $= 100$, and $\Delta Y = 0.5$. With these parameters, the critical jet spacing is $D_c = 1.55$. (a) Five forcing latitudes (initial jet spacing $D_{\text{jet,i}} = 2.4$, bold open circle in Fig. 10(a). (b) Nine forcing latitudes (initial jet spacing $D_{\text{jet,i}} = 1.33$, bold cross in Fig. 10(a). Blue lines indicate critical latitudes ($-1 < \langle U \rangle < -0.99$). Red lines represent locations where the effective β vanishes, $1 - \gamma^{-1}\partial_Y^2\langle U \rangle < 0.01$. On the two right-hand-side panels, the continuous black line is $T = 40$ and the dashed purple line is $T = 2$.

a situation where the curvature of the retrograde flanks is γ, but no critical latitudes form due to the wave forcing being too weak [Fig. 14(c)]. We can calculate again the zonal velocity profile assuming a retrograde curvature of γ, but a minimum velocity larger than -1, $0 > U_{\min} > -1$. We find that

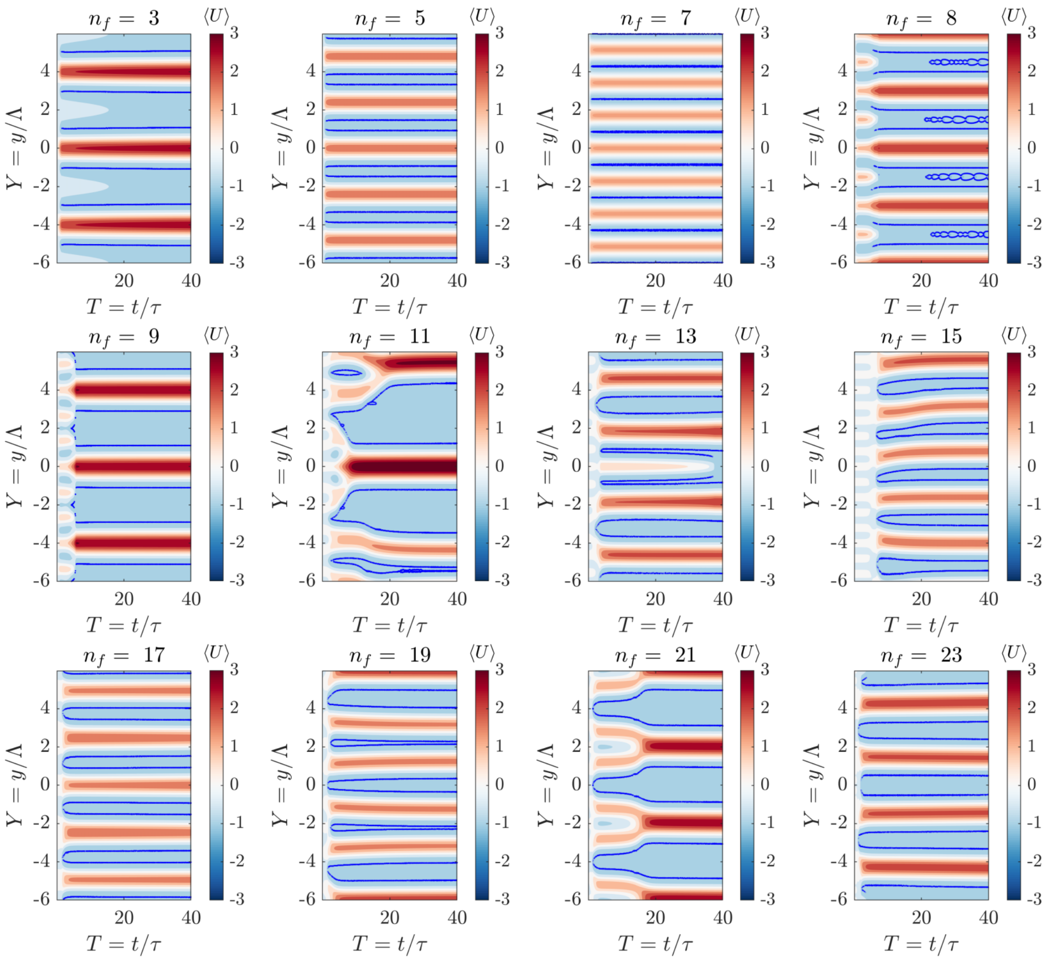

FIG. 8. Parameter sweep with decreasing initial jet spacing ($\gamma = 10$, Re $= 100$, $\Delta Y = 0.5$). The number of forcing latitudes, n_f is indicated at the top of each panel. The initial jet spacing is $D_{\mathrm{jet,i}} = 12/n_f$ and goes from 4 to 0.52. Blues lines indicate critical latitudes ($-1 < \langle U \rangle < -0.99$).

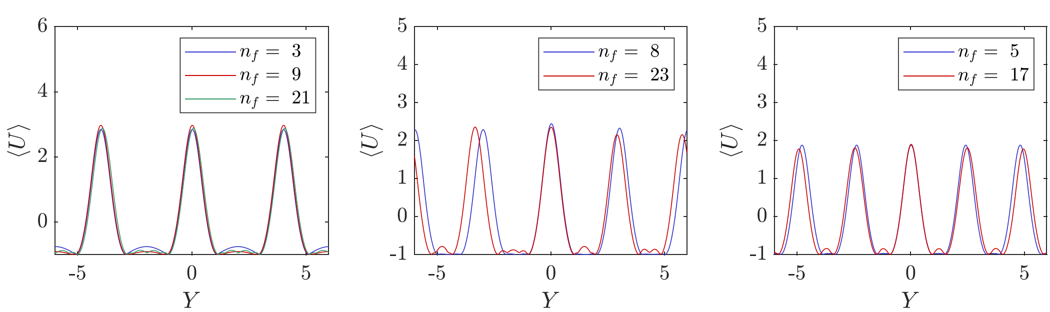

FIG. 9. Comparison of zonal flow profiles with the same final number of equilibrated jets but a different number of forcing latitudes, n_f. The corresponding space-time diagrams are represented in Fig. 8.

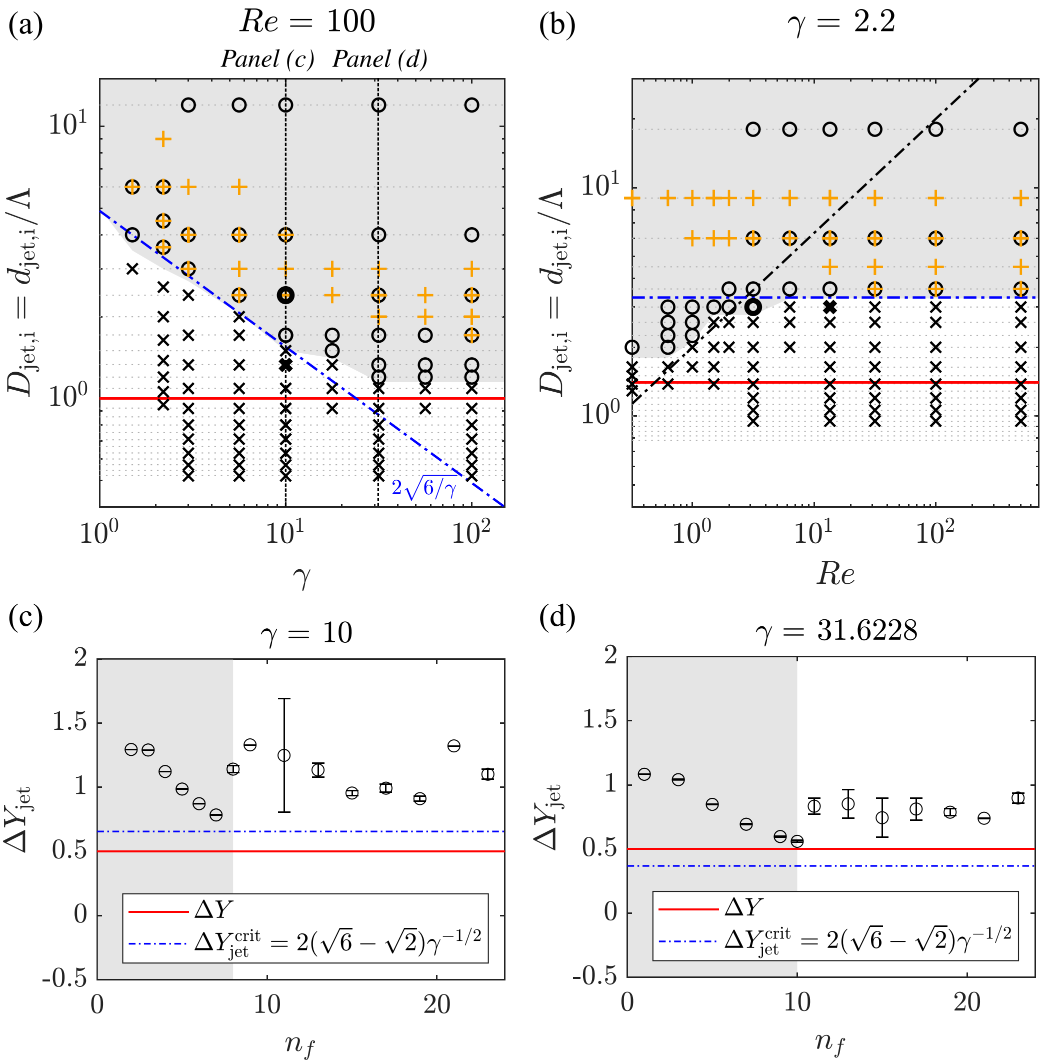

FIG. 10. (a), (b) Stability diagram showing the initial jet spacing versus γ and Re. Since the number of jets is an integer, the initial jet spacing can only take specific values represented by the dashed horizontal lines. The continuous red horizontal line represents a jet spacing of $2\Delta Y$. Circles represent stable cases, where jets remain individual (shaded region). Black crosses represent unstable cases, where jets coalesce. For each black cross, an orange cross shows the new jet spacing after coalescence. There are less orange crosses than black crosses because different forcing latitude numbers might lead to the same number of jets in the equilibrated state. The bold symbols in panel (a) are the two cases shown in Fig. 7. The bold symbols in panel (b) are the two cases shown in Fig. 14. (c), (d) Mean width of the prograde jets as a function of the number of forcing latitudes for the two vertical lines in panel (a). The shaded areas are cases where the jets are individually forced (no coalescence). (c) Case where the minimum jet width is controlled by the curvature ($\Delta Y < \Delta Y_{\text{jet}}^{\text{crit}}$). $\gamma = 10$, Re $= 100$. The jets coalesce when their critical latitudes meet. (d) Case where the minimum jet width is controlled by the forcing width ($\Delta Y > \Delta Y_{\text{jet}}^{\text{crit}}$). $\gamma = 10^{1.5}$, Re $= 100$.

the distance between the retrograde minimum and the prograde maximum is now $D^* = \sqrt{-6U_{\min}/\gamma}$ and $U_{\max} = 2U_{\min}$. The critical distance between two prograde jets such that their retrograde minima overlap becomes $D_c^* = 2\sqrt{-6U_{\min}}\gamma^{-1/2}$. For a small, fixed γ, since $U_{\min} \propto$ Re, we hence expect the critical distance to scale as $D_c^* \propto \text{Re}^{1/2}$ [dashed line in Fig. 10(b)]. The coalescence is therefore predicted to happen at larger jet spacing for larger Re. This is what is observed in Fig. 10(b). Once Re is large enough, critical latitudes form again, and $U_{\min} = -1$ independently of Re, hence the plateau with a critical jet spacing $2\sqrt{6}\gamma^{-1/2}$ (dashed blue line).

C. Comparison with direct numerical simulations

We now proceed to compare the predictions of the WKB model with the fully nonlinear problem. To do so, we solve the forced-dissipative nonlinear barotropic vorticity equation on a β plane:

$$\frac{\partial \zeta}{\partial t} + J(\psi, \zeta + \beta y) = -r\zeta + \sqrt{\varepsilon}\xi, \tag{36}$$

where J is the Jacobian $J(g,h) = (\partial_x g)(\partial_y h) - (\partial_x h)(\partial_y g)$, and ψ is the stream function, i.e., $(u, v) = (-\partial_y \psi, \partial_x \psi)$ and $\zeta = \nabla^2 \psi$. The flow is dissipated with linear damping at a rate $r = 0.01$. An important difference with the quasilinear WKB model is that both the waves and the mean flow are damped by the same term, at the same rate. We prioritized having the same representation of wave damping as in the quasilinear model, hence the choice of linear damping. The forcing term $\sqrt{\varepsilon}\xi$ is a regular stochastic forcing multiplied by a mask in y to mimic random stirring in a narrow region in the meridional direction. The mask is Gaussian, $\exp(-(y/\Delta y_f)^2)$, with $\Delta y_f = 0.139$ [see also Fig. 11(a)]. The stochastic forcing is delta-correlated in time and isotropic. Power is injected in a narrow annulus in wave-number space with total wave number $k_f = 30$ and forcing bandwidth $\delta f = 0.5$. The forcing injects energy per unit area and per unit time equal to $\varepsilon = 10^{-3}$, unless otherwise noted. This flow is simulated using the open-source pseudospectral solver GeophysicalFlows.jl [33] with the timestepper "FilteredRK4," which applies a wave-number filter at every time-step that removes enstrophy at high wave numbers and, thereby, stabilizes the problem. The domain is doubly periodic, $2\pi \times 2\pi$, with resolution 256×256 or 512×512.

In direct numerical simulation (DNS) of β-plane turbulence with small-scale forcing, the strength of the zonation depends on the zonostrophy parameter $R_\beta = 2^{1/2} U^{1/2} \beta^{1/10} \varepsilon^{-1/5}$ [34]. U is the rms velocity of the flow which can be estimated *a priori* by equilibrating energy input with dissipation by friction: $U \sim \sqrt{\varepsilon/r}$. For large zonostrophy index, strong and stable zonal jets are generally found, whereas for small R_β, zonal jets are latent, meander more, and the system is driven further out-of-equilibrium. It has been shown that quasilinear approximations work best when the zonostrophy index is large, typically $R_\beta \gtrsim 2$ [35]. In the DNS of Fig. 12, the zonostrophy index is $R_\beta \approx 4.8$, and for the range of β considered in Fig. 13, $R_\beta \in [3.5, 5.0]$, so we are indeed in the high zonostrophy limit.

Figure 11 shows the early times of a nonlinear DNS with $\beta = 60$, $r = 0.01$, and $\varepsilon = 1 \times 10^{-3}$, with a single forcing latitude located around $y = 0$. Rossby waves that radiate away from the forcing region are visible in Fig. 11(a). Space-time diagrams of the across-jet velocity allow us to measure a clear dominant phase speed $c = -0.095$ as shown in Fig. 11(b). Consistently with theory, this wave radiation leads to momentum convergence toward the source region [Figs. 11(d)–11(f)], inducing a positive mean flow acceleration. The previously made assumption that the Reynolds stresses decay exponentially away from the forcing region is verified in Fig. 11(e). A fit of this exponential decay provides the values of the attenuation distance Λ and the wave forcing amplitude, f_0. The nonlinear simulations hence fully support the structure of the Reynolds stresses obtained from the WKB momentum flux closure (Fig. 1).

Figures 12(a)–12(c) show space-time diagrams of the zonal flow for the same parameters, with an increasing number of forcing latitudes, n_f. The observed behavior is consistent with the quasilinear WKB model: individual wave-driven prograde jets emerge when the forcing latitudes are far from each other, until coalescence occurs under a critical jet spacing (here occurring for $n_f \geqslant 18$). After coalescence, the jets equilibrate at a new scale. In Fig. 12(d), we run a simulation with the same set of parameters, but with a spatially homogeneous forcing. The solution resembles very closely the solution in the case of an inhomogeneous forcing with $n_f = 23$ [Fig. 12(c)], confirming the

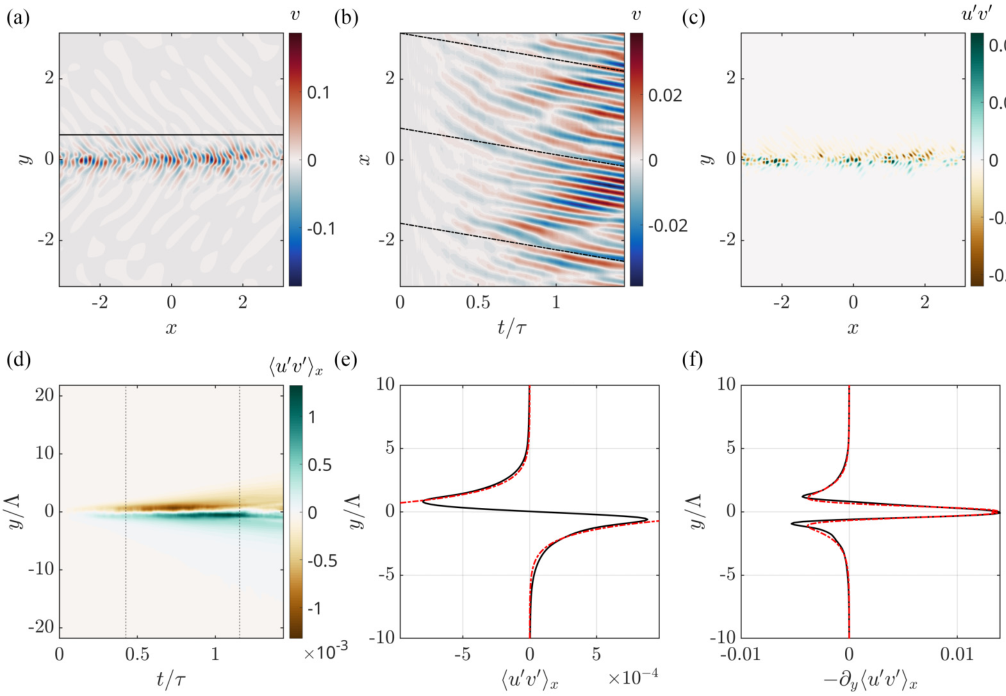

FIG. 11. Numerical solution of the nonlinear barotropic vorticity equation ($\beta = 60$) at early times (transient) with random stirring localized around $y = 0$. (a) Two-dimensional map of the y component of the velocity at time $t/\tau = 1.5$. (b) y component of the velocity as a function of longitude (x) and time. The velocity is measured along a fixed y coordinate represented by a black line in panel (a). The black dashed line corresponds to a propagation velocity of $c = -0.095$. (c) Two-dimensional map of the Reynolds stress ($u'v'$) at time $t/\tau = 1.5$, before zonal averaging. (d) Space-time diagram of the Reynolds stresses. The vertical dotted lines show the time interval over which panels e and f are averaged. (e) Meridional profile of the Reynolds stresses. Red dashed line: theoretical prediction, exponential decay $\pm f_0 \exp(-|y|/\Lambda)$ with $f_0 = 1.97 \times 10^{-3}$ and $\Lambda = 0.14$. (f) Meridional profile of the Reynolds stresses divergence. Red dashed line: theoretical prediction with Gaussian regularization [Eqs. (A13) and (A13)] over a forcing width $\Delta y = 0.083 = 0.59\Lambda$.

hypothesis that under the critical jet spacing, the zonal flow is globally driven and insensitive to the details of the forcing.

From the parameters measured during the transient (Fig. 11), one can calculate the control parameters that should be used to run the corresponding quasilinear WKB cases. Note that in the DNS, there is a single dissipation term, which is a linear damping. For consistency, we ran the quasilinear WKB model with linear damping in the zonal flow equation instead of a viscous damping. In Eq. (32), the term $\frac{1}{\mathrm{Re}}\frac{\partial^2\langle U\rangle}{\partial Y^2}$ is hence replaced by $-\mathrm{Re}_r\langle U\rangle$, and we define the corresponding forcing Reynolds $\mathrm{Re}_r = f_0/(|c|\Lambda r)$. Figures 12(e) and 12(f) show the coalescence obtained in the quasilinear WKB model with parameters determined from the transient of the DNS ($\gamma = 15$ and $\mathrm{Re}_r = 16$). Even though merger events look qualitatively similar, the critical distance at which coalescence occurs is larger in the DNS ($\sim 2.6\Lambda$) compared with the quasilinear WKB model ($\sim 1.4\Lambda$), resulting in a different number of jets after coalescence.

To verify this, we ran nonlinear simulations for a range of values of β and measured the critical jet spacing, as represented in Fig. 13(a). For each of value of β, we estimate the corresponding parameters for the quasilinear WKB model from the transient of the case with one forcing latitude. The critical jet spacing measured from the quasilinear WKB model is represented in Fig. 13(b), as a function of the prediction, $d_c = 2\sqrt{6|c|/\beta}$ (equivalent to $D_c = 2\sqrt{6}\gamma^{-1/2}$). The scaling is confirmed

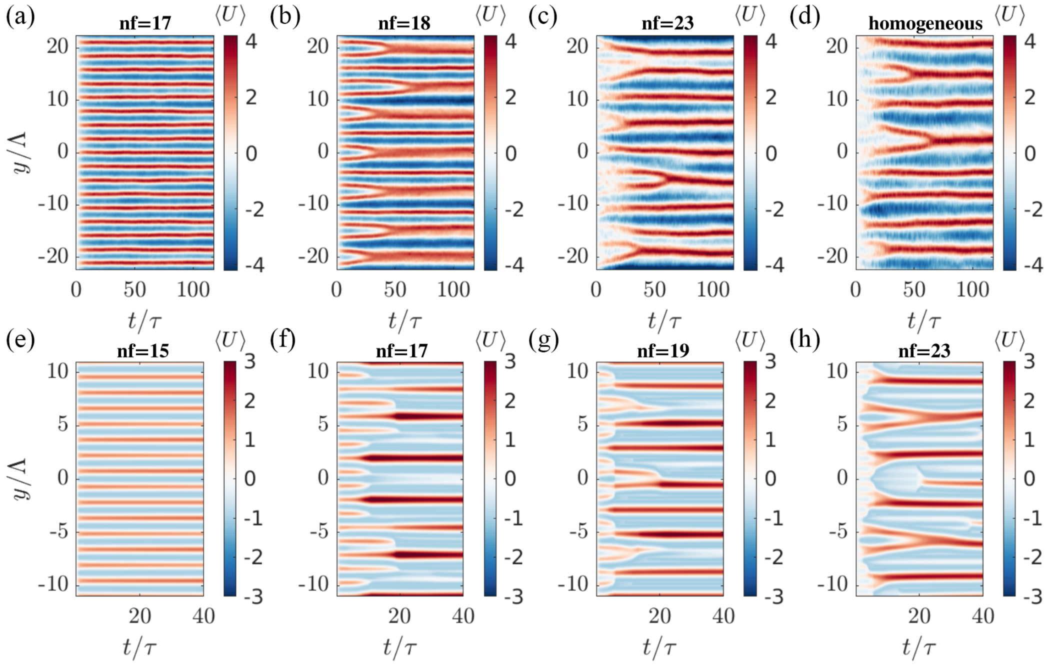

FIG. 12. Comparison between the nonlinear DNS with localized random stirring (top row) and the quasilinear WKB model (bottom row). For both the DNS and the WKB model, $\gamma = 15$ and Re $= 16$. In all panels, n_f is the number of forcing latitudes. Panel (d) has homogeneous (not localized) forcing.

by the nonlinear DNS, but it is offset by a constant value. The quantitative agreement between the fully nonlinear model and the quasilinear asymptotic model is hence only partial. Understanding the origin of the offset will require further investigation.

D. Comparison with experimental observations

The quasilinear WKB model was motivated and inspired by experimental observations reported in Lemasquerier *et al.* [27]. A rapidly rotating tank with a topographic β effect and a small-scale turbulent forcing was used to study the spontaneous emergence of turbulent zonal jets. The forcing consisted in inlets and outlets distributed on a polar array made of six rings. As such, the six rings act as six wave source regions, located at different radii, i.e., different "latitudes." In this setup, a transition between locally and globally forced zonal jets was observed when the amplitude of the forcing was increased, as represented in Figs. 14(a) and 14(b). At low forcing amplitude, six wave-driven jets emerged above each forcing ring. As the forcing amplitude was increased, the amplitude of the six zonal jets increased and they coalesced, leading to a new statistically steady state with fewer (two to three) jets. Lemasquerier *et al.* [27] proposed a linear resonance mechanism to explain the transition in amplitude of the zonal flow and the associated bistability. Their model, however, assumes a uniform background zonal flow, and hence cannot predict changes in the meridional structure of the zonal flow profile. Understanding why the jets merge and equilibrate at a new scale thus remained an open question.

Using particle image velocimetry, Eulerian, time-resolved, velocity fields were measured, including at the very beginning of an experiment where the wave radiation is visible. From these velocity fields, one can measure the Reynolds stress amplitude and their meridional structure (Figs. 9 and 10 in Ref. [27]). Fitting the Reynolds stress profile gives $f_0 \approx 5.15 \times 10^{-6}$ m^2 s^{-2}, $\Delta y \approx 1.15$ cm, $\Lambda \approx 1.65$ cm. The phase speed of forced Rossby waves is $|c| \sim 6.3$ mm/s, the topographic β effect

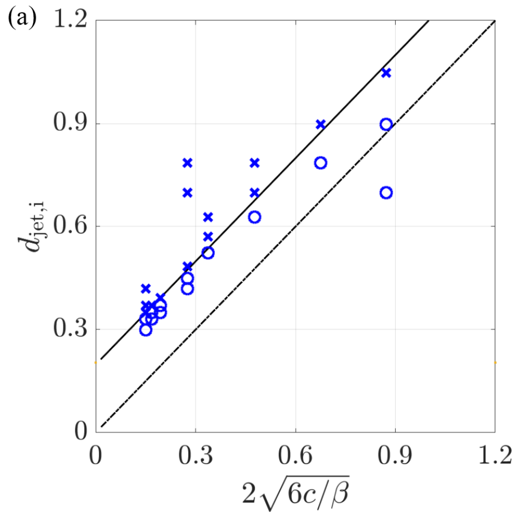

FIG. 13. Critical initial jet spacing for coalescence to occur. Crosses: cases with individual jets. Circles: cases with coalescence. (a) Nonlinear DNS. (b) Quasilinear WKB model. Dashed line: theoretical prediction $d_c = 2\sqrt{6c/\beta}$. Full line: Observed critical distance in the DNS, $d_c = 2\sqrt{6c/\beta} + 0.198$.

is $\beta \approx 50\ \mathrm{m}^{-1}\,\mathrm{s}^{-1}$, and the initial jet spacing is of about 7 cm. The corresponding dimensionless parameters relevant for our quasilinear WKB model are $\gamma = 2.2$, $\mathrm{Re} = 13.5$, $\Delta Y = 0.7$, and $D_{\mathrm{jet,i}} = 4$. Because of relatively strong viscous dissipation, the experiments are in a rather low γ regime, i.e., the Rossby waves are not particularly weakly damped.

The regime diagram of Fig. 10(b) corresponds to the experimental parameter $\gamma = 2.2$. The range of Re on the diagram represents different possible wave forcing amplitudes. For low γ and low Re, our quasilinear WKB model suggests that at a fixed jet spacing, increasing the wave forcing amplitude [from left to right in Fig. 10(b)] leads to a transition between locally driven and globally driven jets. This is consistent with what was observed experimentally. For the parameters considered here, this can happen only if the initial jet spacing is smaller than about 3.3 [dashed blue line in Fig. 10(b)]. This is slightly smaller than the estimated value estimated from the experiment, $D_{\mathrm{jet,i}} = 4$, but quite surprisingly close given the uncertainty in experimental parameters and approximations of the QL model compared to the fully three-dimensional turbulent experiments. Furthermore, the range of Re over which such transition occurs is quantitatively consistent with the experiment.

To illustrate the experimental case with the quasilinear WKB model, we force 6 jets over a periodic domain of length $L = 18$ ($D_{\mathrm{jet,i}} = 3$) and we increase Re from $10^{1/2}$ to 13.5 to simulate an increase in the wave forcing amplitude. This corresponds to going from the bold circle to the bold cross in Fig. 10(b). Results are shown in Figs. 14(c) and 14(d). At low Re (so-called Regime I in Lemasquerier *et al.* [27]), six independent jets are formed, separated by regions of low effective β. We note that, as mentioned earlier, no critical latitudes form because of the small Re and small γ. At high Re (so-called Regime II), all parameters being the same, the system transitions to a state with 3 jets separated by critical latitudes. The transition is accompanied by an increase in the prograde jets amplitude both because of the increased wave forcing (increased Re), and because the jets amplitude increase when they coalesce into fewer jets. This qualitatively reproduces well the experimental observations. The time over which the transition occurs, of the order of 40 streaming times, is comparable in the model and the experiment (Fig. 14).

For completeness, we run the equivalent nonlinear simulations ($\beta = 20$, $r = 0.01$) with $n_f = 7$ forcing latitudes on a domain $\pi \times \pi$. The measured attenuation distance on the transient is

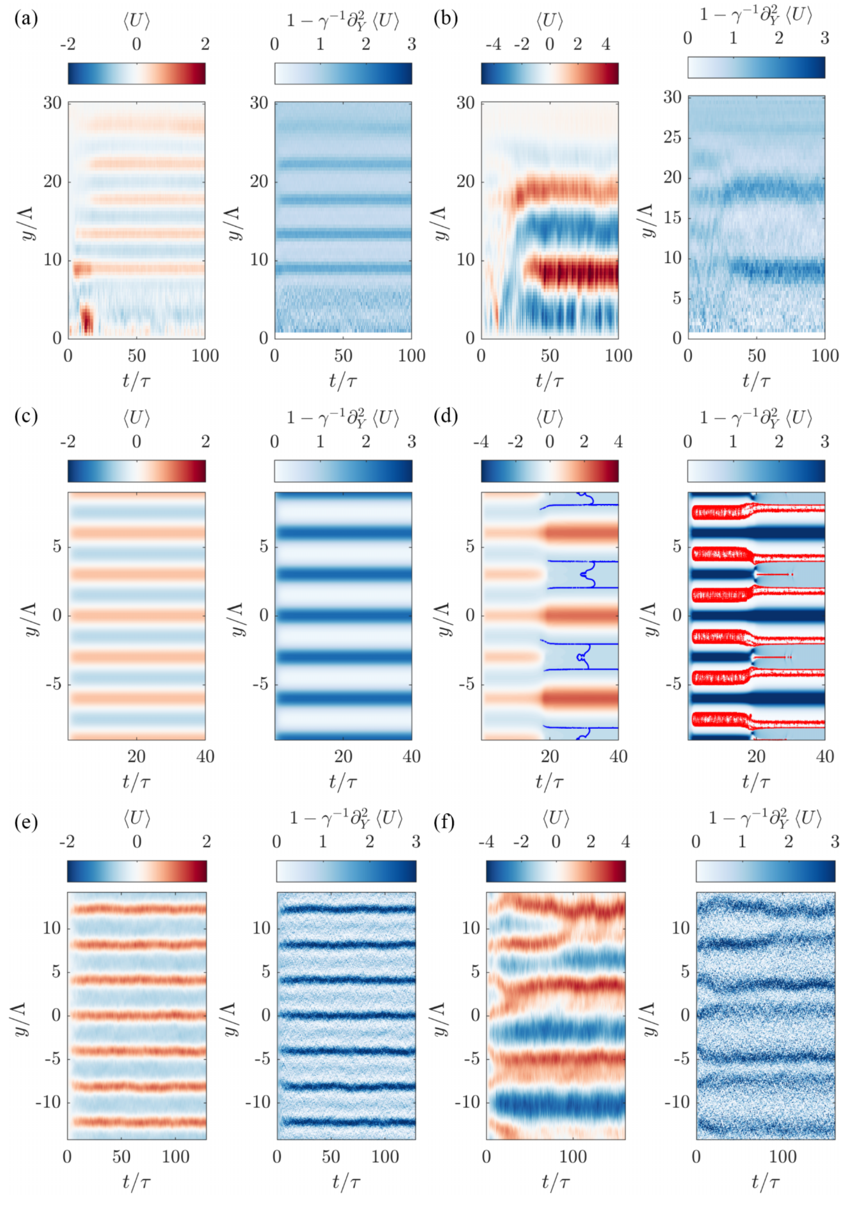

FIG. 14. (a), (b) Experimental results of Lemasquerier *et al.* [27] showing space-time diagrams of the zonal flow and effective β effect for two regimes. Experimental parameters are estimated to be $\gamma = 2.2$, $\mathrm{Re} = 13.5$, $\Delta Y = 0.7$ and $D_{\mathrm{jet,i}} = 4$. (a) Regime observed at low forcing amplitude (locally driven jets). There are six equidistant forcing rings in the experiment, one beneath each prograde jet. (b) Regime observed at high forcing amplitude (globally driven jets). (c), (d) Quasilinear WKB model with $\gamma = 2.2$, $\Delta Y = 0.7$, and initial jet spacing $D_{\mathrm{jet,i}} = 3$. (c) Regime of individual jets. $\mathrm{Re} = 10^{1/2}$ [bold open circle in Fig. 10(b)]. (d) Regime of coalescence. $\mathrm{Re} = 13.5$ [bold cross in Fig. 10(b)]. (e), (f) Nonlinear DNS with $\beta = 20$, $r = 0.01$, $\Delta Y = 0.75$, and initial jet spacing $D_{\mathrm{jet,i}} = 4$. (e) $\varepsilon = 1 \times 10^{-4}$, corresponding to $\gamma = 16.8$ and $\mathrm{Re}_r = 4.2$. (f) $\varepsilon = 1 \times 10^{-3}$, corresponding to $\gamma = 2.7$ and $\mathrm{Re}_r = 15.7$.

$\Lambda = 0.11$, giving an initial jet spacing of $d_{\mathrm{jet,i}} = 4\Lambda$ as in the experiment. We increase the forcing energy input rate from $\varepsilon = 1 \times 10^{-4}$ [Fig. 14(e)] to $\varepsilon = 1 \times 10^{-3}$ [Fig. 14(f)]. This corresponds to increasing Re_r from 4.2 to 15.7. Increasing the forcing amplitude leads again to a transition from seven locally driven jets to coalescence into 3 broader jets of similar amplitude and width compared with the experiment.

IV. DISCUSSION

A. Relevance for planetary applications

Our quasilinear model is able to describe situations where zonal jets are locally driven by a wave source, and situations where the wave forcing is "homogeneous" due to the distance between wave sources being below the critical distance for coalescence. We discuss potential implications for different jet problems, and then make estimates of the critical jet spacing predicted by our model in the case of a homogeneous forcing.

There are many examples in natural flows where the forcing is spatially localized, particularly in the Earth's oceans and atmosphere [36,37]. For instance, the Azores current is currently understood as being caused by the localized sink in the Mediterranean outflow [38]. Transport of angular momentum by a localized Rossby wave source is also key to understand eddy-driven jets in the Earth's atmosphere [18,37]. In this case, Rossby waves are radiated by topographic forcing or baroclinic instabilities acting as a wavemaker, and this process sustains, for instance, the eddy-driven midlatitude jet stream. Even though the present work focuses on midlatitude dynamics, transport of angular momentum by locally forced waves is also crucial to maintain prograde equatorial jets (superrotation) on Venus, Titan, Jupiter, Saturn, and the huge range of exoplanets being discovered. Possible equatorial "wavemakers" include a Rossby-Kelvin instability for Venus and Titan [39,40], convection on gas giants [41], and inhomogeneous thermal forcing on tidally locked exoplanets [42]. Finally, the convergence of vertical fluxes of momentum (instead of meridional ones) due to the upward propagation of gravity waves leads to the Earth's QBO. In the inhomogeneous case, with localized wave sources, our quasilinear model hence extends classical material on how Rossby wave radiation leads to the formation of zonal jets.

If the forcing region has an *extended* meridional extent, then multiple zonal jets can form within it, as in the case of gas giants. This would correspond to our coalescence regime, where, as wave sources are pushed closer together, the extent of the forcing region becomes the entire domain. This hypothesis is supported by the fact that below the coalescence threshold, the zonal flow shows hint of universal behavior and reaches an equilibrium flow with jets separated by a Rhines scale. We estimate below a critical jet spacing for planetary flows with multiple jets, and show that these are consistent with observations.

On Jupiter, there are several observational evidence of latitudinally trapped planetary scale waves, interpreted as equatorial Rossby waves [e.g., 43,44]. For instance, Arregi *et al.* [44] studied the motion of hot spots at 7°N on Jupiter, and used the theoretical dispersion relation to interpret them as Rossby waves with zonal wave numbers 8–12, Doppler-shifted phase speed of 97–113 m/s, propagating on a background flow of 140 m/s. Li *et al.* [45] described observations of a longitudinal wave pattern centered around 14.5°N (North-Equatorial Belt, NEB), and argue that the NEB wave is a recurring phenomenon, already observed by Orton *et al.* [46] and Simon-Miller *et al.* [47]. It was subsequently identified from thermal data [48,49]. The interested reader can find a chronology of mid-NEB wave detections in the supplementary information of Fletcher *et al.* [49]. On Saturn, Gunnarson *et al.* [50] analyzed the motion of three ribbon waves around 42°N and showed that their wavelengths and propagation are consistent with primarily barotropic Rossby waves propagating westward relatively to a mean wind speed of 54.8 m/s. We report some of these observations in Table I.

The validity of the assumptions behind our quasilinear WBK model can be estimated from these observations. The timescale separation between fluctuations and mean flow on gas giants is well

TABLE I. Data used for estimating the critical jet spacing on gas giants and Earth oceans. The β effect is estimated at the latitude indicated in parenthesis for each case following $\beta \sim 2\Omega/R\cos(\theta)$. Rossby wave phase speeds and wave numbers are taken from references in brackets.

	Ω (rad/s)	R (km)	β ($\mathrm{m^{-1}s^{-1}}$)	k (rad/m)	$\lvert c\rvert$ (m/s)	d_c (km) [° lat]
Jupiter (7°N) [44]	1.76×10^{-4}	69,911	4.9×10^{-12}	$\sim1.8\times10^{-7}$	27–43	11 500–14 500 [9.4–11.9°]
Saturn (42°N) [50]	1.66×10^{-4}	58,232	4.4×10^{-12}	$\sim1.4\times10^{-6}$	10–35	7700–14 500 [7.6–14.3°]
Earth oceans [54]	7.29×10^{-5}	6371	2.0×10^{-11}	–	2×10^{-2}	150 [2°]

established. Fluctuating vortices on Jupiter evolve on a timescale of a few days [51], whereas zonal winds evolve on timescales of 100 to 10 000 Jovian days. This fully justifies adopting a quasistatic approach where waves see a frozen-in-time zonal flow. The weak damping limit, required in the WKB approximation, is valid in the limit $r \ll k|c|$. Using data from Arregi *et al.* [44] (Table I), this leads to the condition $r \ll 5\times10^{-6}\ \mathrm{s^{-1}}$, i.e., a damping time that should be much larger than about 56 h, which is very likely to be the case. For instance, the atmospheric radiation model of Li *et al.* [52] gives Newtonian cooling rates of the order of 10^{-9}–$10^{-7}\ \mathrm{s^{-1}}$ for Jupiter. The weak damping limit $\gamma \gg 1$ is hence justified. In terms of the forcing, with measured Reynolds stress amplitude $f_0 \sim 10\ \mathrm{m^2\,s^{-2}}$ [53], an eddy diffusivity $\nu \sim 1\times10^{-2}\ \mathrm{m^2\,s^{-1}}$ and an attenuation distance $\Lambda \sim 23,000$ km (corresponding to the limiting case $r \sim 5\times10^{-6}\ \mathrm{s^{-1}}$), we are in the limit $\mathrm{Re} = f_0\Lambda/(\nu|c|) \gg 1$.

In a natural turbulent flow such as Jupiter's atmosphere, we assume the wave forcing to be distributed randomly in latitude, due for instance to deep convection, moist convection in the weather layer, or baroclinic instabilities. Hence, the "coalescence" regime is the relevant regime to look at to understand the final zonal jets equilibrium. To check if observations support our model, we can look at if the observed distance between two prograde jets is of order of the critical jet spacing, below which jets are predicted to coalesce in our model. In the limit $\gamma \gg 1$ and $\mathrm{Re} \gg 1$, that critical distance is $2\sqrt{6/\gamma}$. In dimensional quantities, this is a Rhines scale, $d_c = 2\sqrt{6|c|/\beta}$, where the relevant velocity to use is that of Rossby waves. Table I and Fig. 15 provide estimates for d_c for Jupiter, Saturn, and Earth's oceans based on Rossby wave observations. Note that oceans on

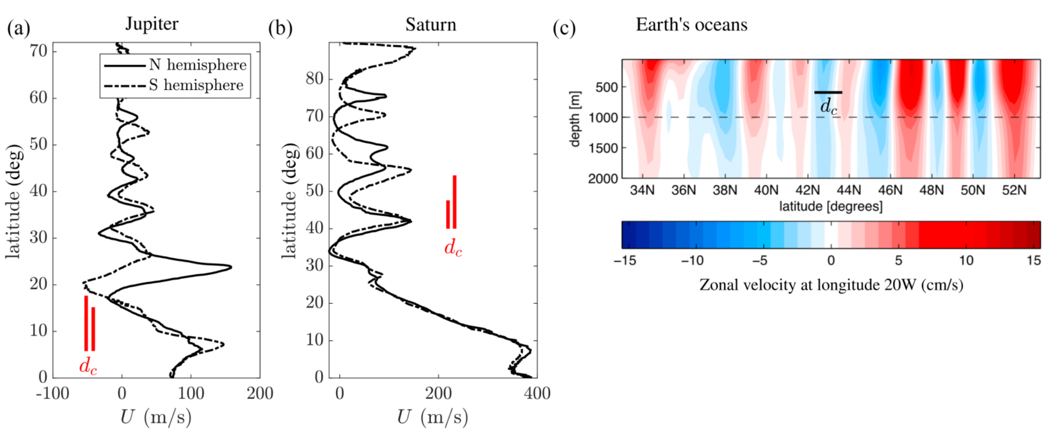

FIG. 15. (a), (b) Zonal winds profiles in both hemispheres of Jupiter (in 2016) and Saturn (average from 2004 to 2009). The data are taken from Tollefson *et al.* [55] for Jupiter and from García-Melendo *et al.* [56] for Saturn. (c) Quasizonal jets in the Northeast Atlantic measured with Argo floats data for 2004–2006 (adapted from Ref. [57]). In all panels, the range of calculated critical jet spacing d_c is represented as vertical bars. Corresponding data is provided in Table I.

Earth are in a different turbulent zonal jet regime compared to gas giants, where zonal jets are weaker and meandering. Nevertheless, the same exercise can be done using Rossby wave data from Klocker and Marshall [54], who measured the zonal propagation speed of ocean eddies and showed that they agree with Doppler-shifted Rossby waves. Figure 15 shows that the obtained critical distances are consistent with the observed separation distance between prograde jets for Jupiter, Saturn and Earth's oceans.

B. Conclusion and future work

We have presented a one-dimensional quasilinear WKB closure to model zonal jets emergence and coalescence on a β plane from the framework of wave-mean flow interactions. This model is motivated from experimental observations [27], and derived in the spirit of the Holton-Lindzen-Plumb model for mean flow reversals in the Earth's stratosphere [26]. It is built on the hypothesis that Rossby wave-zonal flow interactions can account for the long-term dynamics and equilibration of zonal flows. To close the zonal flow equation, an explicit expression for the Reynolds stress divergence was obtained, assuming that it is due to the emission and attenuation of Rossby waves, i.e., a streaming process. The momentum flux closure obtained under a WKB approximation incorporates two crucial feedback effects of the zonal flow on the propagation of the waves: the Doppler shift of the waves and the modification of the background planetary β effect due to the curvature of the zonal flow. The consequences of these feedback effects are (1) the emergence of critical latitudes, where the zonal flow speed matches the phase speed and the wave momentum flux vanishes, and (2) the emergence of turning latitudes, regions of vanishing effective β in retrograde flows.

We integrated the closed zonal flow evolution equation in time with multiple latitudes of wave emission. We showed that when wave-driven prograde jets are forced close enough together, there is a transition between a regime where the jets are *locally driven* to a regime where the jets coalesce and become *globally driven*. This second regime is arguably the one relevant to gas giants applications, where the flow supports a sea of Rossby waves, with no preferred forcing regions, i.e., it is a model for a homogeneous forcing situation. We showed that in the limit of weak wave damping ($\gamma \gg 1$), the coalescence transition occurs when the critical latitudes on the flanks of adjacent prograde jets overlap. Since the position of the critical latitudes is controlled by the maximum curvature of the retrograde flanks (β), this translates into a critical jet spacing $d_c = 2\sqrt{6|c|/\beta}$ (large wave streaming, $\mathrm{Re} \gg 1$), or $d_c = 2\sqrt{6|U_{\min}|/\beta}$ in the cases where critical latitudes do not form (weak wave streaming, $\mathrm{Re} \sim 1$ and $\gamma \sim 1$). Hence, our closure naturally leads to an equilibrium flow with jets separated by a Rhines scale.

At this point, it is worth mentioning differences between our model and the closure previously proposed by Srinivasan and Young [12] (SY14 hereafter), Woillez and Bouchet [14] (WB19), and Jackman and Esler [13] (JE23). SY14, WB19, and JE23 adopt a closure aiming at representing small-scale random forcing of the flow, i.e., the Reynolds stresses are derived assuming a spatially homogeneous weak stochastic forcing. In contrast, we consider a deterministic forcing due to a *localized* and *monochromatic* Rossby wave source. Our forcing is spatially inhomogeneous, even though our hypothesis is that when forcing latitudes are close enough together, we retrieve what would be obtained for a homogeneous forcing.

The second difference (perhaps the most important one) is that SY14, WB19, and JE23 are *local* closure theories, assuming that the mean flow can be locally approximated as a linear shear flow. This approach is analogous to what has been done for the vortex condensate problem considered by, e.g., Laurie *et al.* [15]. It leads to a theoretical expression for Reynolds stress that depends only on the zonal flow shear U_y and does not depend on β nor the mean flow curvature. The zonal flow is therefore necessarily monotonic, there are no turning latitudes where $\beta - U_{yy} = 0$, and it leads to a symmetry between prograde and retrograde jets. That being said, JE23 extended SY14 and showed that their closure is in fact accurate even near jet extrema, as long as the flow is strongly relaxed to an alternating *stable* jet profile (no barotropic instability). They show that SY14 is, however, not accurate in the general case of an equilibrated jet flow in β-plane turbulence because of the secondary momentum fluxes due to barotropic instabilities that are important near the jet extrema, and so far, these momentum fluxes have not been successfully parametrized.

In contrast, our approach is fundamentally *nonlocal* since we build the Reynolds stress from the nonlocal nature of Rossby wave propagation and attenuation. The wave flux at any latitude depends on the cumulative zonal wind profile at the latitudes covered previously, as implied by the integral over latitude in Eq. (16). In our model, the zonal flow is not monotonic, and both critical latitudes and turning latitudes are free to develop once the zonal flow equation is evolved in time. In particular, the retrograde jets curvature cannot exceed β, making them marginally unstable to the barotropic instability by construction. This maximum curvature naturally leads to an equilibrium zonal flow profile with jets separated by a Rhines scale. This also leads to an asymmetry between prograde and retrograde jets, with retrograde jets closer to a parabolic profile whereas prograde jets have a cusp, as often observed in natural systems. To the best of our knowledge, this is the first purely zonal closure model that self-consistently leads to this result. Note that the nonlocal nature of our closure is not incompatible with the picture of zonostrophic turbulence, where both local cascades and nonlocal direct energy transfers coexist [58].

One of the aim of our model is to provide a tool to bridge the gap between theories of jets arising from localized wave sources, a common situation in terrestrial atmospheres [37] and oceans [36], and globally driven jets arising from a homogeneous forcing, a situation relevant for gas giants and convective cores. Our model is able to predict a transition between these two regimes, essentially by moving wave sources close enough together until coalescence of wave-driven jets occurs. Our model quantitatively predicts the transition from locally to globally driven jets observed experimentally by Lemasquerier *et al.* [27]. The obtained number of jets is comparable, as well as the time necessary for the transition to occur. Furthermore, our systematic study shows that the regime where jets coalesce shows hints of a universal behavior, where the properties of the jets become independent of the forcing detail, an indication that this could indeed be a good representation of a homogeneous forcing situation. The key idea in this regime is that although the wave forcing is homogeneous, the momentum transport is not and is organized into a banded structure, with wave–momentum convergence into prograde (eastward) jets and wave-momentum divergence in retrograde (westward flows). In other words, the important point is that the wave *dissipation* is heterogeneous, with waves preferentially attenuated in retrograde flows. This heterogeneous dissipation, arising due to the feedback of the zonal flow, is precisely why zonal jets emerge in stochastically forced DNS, even when the forcing is homogeneous.

Our quasilinear model is hence a typical example of how small scale/fast processes (here, Rossby waves) can be parametrized, but still retain effects that are essential to the large scale/slow dynamics (here, zonal jets). It helps to extract the minimum ingredients necessary for jet formation and coalescence: (1) Rossby wave sources, (2) modified wave attenuation due to the Doppler shift and the modification of the PV gradient by the zonal flow, and (3) direct nonlinear exchange of momentum between the waves and the mean flow, neglecting triad interactions. Although several factors support the relevance of the model, it remains an idealized quasilinear model. Comparison with fully nonlinear DNS shows only partial quantitative agreement, which deserves to be further investigated. An area of improvement would be to consider a polychromatic wave forcing accounting for multiple wave numbers, instead of a monochromatic one, as was done for the Holton-Lindzen-Plumb model [59].

Beyond offering insights into the underlying physical mechanisms, the ability to parametrize the Reynolds stress holds great promise for modelers. To investigate the long-term dynamics of jet flows, one must evolve the system over very long timescales while still resolving the short temporal and spatial scales of the fluctuations. Closure models can dramatically reduce computational costs by replacing a fully two-dimensional nonlinear DNS with a one-dimensional zonal flow equation, in which only the slow, large-scale dynamics need to be resolved. Such savings could make it easier to explore long-term behavior such as drift, rare transitions between multistable states, or to conduct more comprehensive parametric studies.

ACKNOWLEDGMENTS

We thank Navid Constantinou for help in setting up GeophysicalFlows.jl. D.L. acknowledges support from the Royal Society via Research Grant No. RGR1241426 and from UKRI via a Future Leaders Fellowship (Grant No. MR/Y01605X/1).

DATA AVAILABILITY

The data that support the findings of this article are openly available [60].

APPENDIX A: HOMOGENEOUS CASE: NO BACKGROUND ZONAL FLOW

The homogeneous case, $\langle u\rangle = 0$, does not require a WKB expansion and is physically insightful. We provide an alternative derivation in this Appendix. In the absence of zonal flow and in the weak damping and large zonal wavelength limits, the wave equation is Eq. (9) with the modified meridional wave number

$$l^2 \approx -\frac{\beta}{c}\left(1 - \mathrm{i}\frac{r}{kc}\right). \tag{A1}$$

Let us consider a northward propagating Rossby wave emitted from the latitude $y = 0$. We search for a solution under the form

$$\tilde{\psi}(y) = \tilde{\psi}_0 \exp\left(\mathrm{i}l_0 y - \frac{y}{2\Lambda}\right). \tag{A2}$$

Substituting in the differential equation, we obtain at leading order in r/kc (weak dissipation)

$$\Lambda = \frac{|k||c|^{3/2}}{r\beta^{1/2}}, \tag{A3}$$

$$l_0 = \pm\sqrt{\frac{\beta}{|c|}}. \tag{A4}$$

The Reynolds stresses due to this wave field can be worked out from the stream function:

$$\langle u'v'\rangle = \langle -\partial_y\psi'\partial_x\psi'\rangle \tag{A5}$$

$$= -\left\langle\left(\frac{d\tilde{\psi}}{dy}e^{ik(x-ct)} + \frac{d\tilde{\psi}^*}{dy}e^{-ik(x-ct)}\right)\left(ik\tilde{\psi}e^{ik(x-ct)} - ik\tilde{\psi}^*e^{-ik(x-ct)}\right)\right\rangle \tag{A6}$$

$$= -ik\left(\tilde{\psi}\frac{d\tilde{\psi}^*}{dy} - \tilde{\psi}^*\frac{d\tilde{\psi}}{dy}\right), \tag{A7}$$

where a star denotes the complex conjugate. With the solution (A2), we obtain

$$\langle u'v'\rangle = -2kl_0\tilde{\psi}_0^2\, e^{-y/\Lambda} = \pm f_0\, e^{-y/\Lambda}, \tag{A8}$$

where

$$f_0 = \frac{2|k|\beta^{1/2}}{|c|^{1/2}}\tilde{\psi}_0^2 \tag{A9}$$

is the Reynolds stresses amplitude due to the waves radiation and will be called the forcing amplitude hereafter. For a wave propagating northward, a positive meridional group velocity [Eq. (12)] requires $kl_0 > 0$, hence the Reynolds stresses are negative, whereas for a southward propagating wave, $kl_0 < 0$ and the Reynolds stresses are positive. In the case of waves propagating away (both northward and southward) from a forcing latitude $y = 0$ [Fig. 1(a)], we therefore have

$$\langle u'v'\rangle^+ = -f_0\, e^{-|y|/\Lambda}, \quad \text{for } y > 0, \tag{A10}$$

$$\langle u'v'\rangle^- = +f_0\, e^{-|y|/\Lambda} \quad \text{for } y < 0, \tag{A11}$$

where the superscript + denotes the northward wave, and − the southward wave [purple curves in Fig. 1(b)]. The divergence of the Reynolds stresses, alternatively called the streaming force, is negative for both the northward and southward wave, as represented in Fig. 1(c):

$$-\frac{\partial}{\partial y}\langle u'v'\rangle^\pm = -\frac{f_0}{\Lambda}\, e^{-|y|/\Lambda}, \quad \text{for } y \neq 0. \tag{A12}$$

Physically, the negative Reynolds stresses divergence arises from the westward phase speed of Rossby waves, which deposit westward momentum when they dissipate. The corresponding streaming force is negative, i.e., a retrograde flow is accelerated away from the forcing region.

At the forcing latitude, the Reynolds stresses do a negative jump of $-2f_0$. The Reynolds stresses divergence would then be $-\partial_y\langle u'v'\rangle = 2f_0\delta(y)$ where δ is the Dirac distribution. This is not physical as it would correspond to an infinite prograde acceleration of the zonal flow at $y = 0$. Instead, we regularize this prograde acceleration over a Gaussian of finite width, Δy, such that its integral over the domain is $2f_0$:

$$-\frac{\partial}{\partial y}\langle u'v'\rangle^0 = \frac{2f_0}{\sqrt{\pi}\,\Delta y}\exp\left(-\left(\frac{y}{\Delta y}\right)^2\right). \tag{A13}$$

This regularization is represented by the red curves in Figs. 1(b) and 1(c). Doing so, we introduce a new free parameter, the width of the forcing region Δy. The larger the forcing region, the smaller the amplitude of the prograde acceleration in the forcing region.

APPENDIX B: MATHEMATICAL DERIVATION OF THE WKB CLOSURE

1. WKB expansion

The goal of this Appendix is to derive a WKB solution for the wave equation (9), find an explicit expression for the Reynolds stresses divergence as a function of the zonal flow, and justify the expression of the modified meridional wave number (11).

We start by deriving the nondimensional version of the wave equation by using the attenuation distance Λ as a length scale, $|c|$ as a velocity scale and we denote nondimensional variables with capital letters:

$$x \to X\Lambda, \quad y \to Y\Lambda, \quad t \to T\Lambda/|c|, \tag{B1}$$

$$(\langle u\rangle, u', v') \to (\langle U\rangle, U', V')|c|, \quad \psi \to \Psi\Lambda|c|. \tag{B2}$$

The wave equation (9) becomes

$$\frac{d^2\tilde{\Psi}}{dY^2} + L^2(Y)\tilde{\Psi} = 0, \tag{B3}$$

with L^2 the rescaled local meridional wave number:

$$L^2(Y) = L_u\left(\gamma - \frac{\partial^2 L_u^{-1}}{\partial Y^2}\right)\left(1 + \gamma^{-1}L_u^2\right)^{-1}\left(1 + \mathrm{i}\gamma^{-1/2}L_u\right) - \eta^2, \tag{B4}$$

and

$$L_u = \frac{1}{\langle U\rangle + 1}. \tag{B5}$$

L_u quantifies the ratio of the waves phase speed without and with a zonal flow. The dissipation of the waves is quantified by the damping parameter,

$$\gamma = \left(\frac{kc}{r}\right)^2 = \frac{\beta\Lambda^2}{|c|}. \tag{B6}$$

Finally, $\eta = \Lambda k$ is the dimensionless zonal wave number and will be considered small in the following (large zonal wavelength).

We adopt a *weak damping limit* ($r \ll kc$), corresponding to a large wave damping parameter ($\gamma \gg 1$). This limit implies a scale separation between the attenuation distance (Λ) and the meridional wavelength of the waves ($\sqrt{|c|/\beta}$). We additionally assume $L_u\gamma^{-1/2} \ll 1$, and we define the small parameter $\epsilon = \gamma^{-1/2}L_u$ which leads to

$$L^2(Y) = \frac{L_u^3}{\epsilon^2}\left(1 - \frac{\epsilon^2}{L_u^2}\frac{\partial^2 L_u^{-1}}{\partial Y^2}\right)(1+\epsilon^2)^{-1}(1+\mathrm{i}\epsilon) - \eta^2. \tag{B7}$$

We assume that the azimuthal wave number is negligible compared to the meridional one ($L^2 \gg \eta^2$), i.e., we consider the long wavelength limit in the azimuthal direction and drop the term η^2. We then expand the $(1+\epsilon^2)^{-1}$ term in powers of ϵ:

$$L^2(Y) = \frac{L_u^3}{\epsilon^2}\left(1 - \frac{\epsilon^2}{L_u^2}\frac{\partial^2 L_u^{-1}}{\partial Y^2}\right)(1-\epsilon^2 + O(\epsilon^4))(1+\mathrm{i}\epsilon). \tag{B8}$$

The second-order Y derivative appearing in this expression of the meridional wave number physically represents the modification of the background β effect by the zonal flow curvature. Here, we argue that this term is *a priori* of of same order as β, i.e., that

$$B(Y) = \frac{\epsilon^2}{L_u^2}\frac{\partial^2 L_u^{-1}}{\partial Y^2} = O(1), \tag{B9}$$

an assumption that will be verified a posteriori. We keep terms up to order ϵ^{-1} in the expression of the meridional wave number, leading to

$$L^2(Y) = \frac{L_u^3}{\epsilon^2}[(1 - B(Y))(1+\mathrm{i}\epsilon) + O(\epsilon^2)]. \tag{B10}$$

Going back to the (L_u, γ) variables, we obtain

$$L^2(Y)\frac{\gamma^{-1}}{L_u} = 1 - B(Y) + \mathrm{i}(1-B(Y))L_u\gamma^{-1/2} + O((L_u\gamma^{-1/2})^2). \tag{B11}$$

Substituting the expression of the meridional wave number into the wave equation (B3) leads to

$$\frac{1}{\gamma}\frac{d^2\tilde{\Psi}}{dY^2} + M^2(Y)\tilde{\Psi} = 0, \tag{B12}$$

where

$$M^2(Y) = M_0^2 + \gamma^{-1/2}M_1^2 + O((\gamma^{-1/2})^2), \tag{B13}$$

$$M_0^2 = L_u(1 - B(Y)), \tag{B14}$$

$$M_1^2 = \mathrm{i}L_u^2(1 - B(Y)). \tag{B15}$$

Guided by the form of the analytical solution if M was a constant, we seek a solution for the amplitude of the Rossby waves $\tilde{\Psi}$ under the form

$$\tilde{\Psi}(Y) = \exp\left(\gamma^{1/2}g(Y)\right). \tag{B16}$$

Injecting this ansatz into Eq. (B12), we obtain a differential equation for g:

$$\gamma^{-1/2}g'' + g'^2 + M^2 = 0. \tag{B17}$$

Let $g = \int_Y h$, then

$$\gamma^{-1/2}h' + h^2 + M^2 = 0. \tag{B18}$$

We expand h in successive powers of $\gamma^{-1/2}$,

$$h = h_0 + \gamma^{-1/2}h_1 + \gamma^{-1}h_2 + \gamma^{-3/2}h_3 + \cdots ,$$

substitute this expansion in the differential equation and collect similar orders in $\gamma^{-1/2}$ (up to order $\gamma^{-1/2}$).

Order γ^0

$$h_0^2 + M_0^2 \;=\; 0, \tag{B19}$$

$$\Rightarrow h_0(Y) = \pm \mathrm{i}\, M_0(Y) = \pm \mathrm{i} L_u^{1/2}(1 - B(Y))^{1/2}. \tag{B20}$$

Order $\gamma^{-1/2}$

$$h_0' + 2h_0h_1 + M_1^2 \;=\; 0, \tag{B21}$$

$$\Rightarrow h_1 = -\frac{1}{2}\frac{h_0'}{h_0} - \frac{M_1^2}{2h_0} \tag{B22}$$

$$\Rightarrow h_1 = -\frac{1}{2}\,\frac{d}{dY}\left[\ln\left(\frac{h_0(Y)}{h_0(0)}\right)\right] \pm \frac{1}{2}L_uM_0(Y) \tag{B23}$$

$$\Rightarrow h_1 = -\frac{1}{2}\frac{d}{dY}\left[\ln\left(\frac{M_0(Y)}{M_0(0)}\right)\right] \pm \frac{1}{2}L_uM_0(Y). \tag{B24}$$

This yields to the final WKB solution for the meridional amplitude of the wave:

$$\begin{aligned}
\tilde{\Psi}(Y) &= \tilde{\Psi}_0 \exp\left[\gamma^{1/2}\int h_0 dY + \int h_1 dY\right] \\
&= \tilde{\Psi}_0 \exp\left[\gamma^{1/2}\int \pm \mathrm{i}\, M_0(Y)dY\right] \exp\left[-\frac{1}{2}\ln\left(\frac{M_0(Y)}{M_0(0)}\right) \pm \frac{1}{2}\int L_uM_0(Y)\right] \\
&= \tilde{\Psi}_0 \left(\frac{M_0(Y)}{M_0(0)}\right)^{-1/2} \exp\left[\pm \mathrm{i}\int\; M_0(Y)d(Y\gamma^{1/2}) \pm \frac{1}{2}\int L_u^{3/2}(1 - B(Y))^{1/2}dY\right].
\end{aligned} \tag{B25}$$

2. WKB closure for the Reynolds stresses

The nondimensional Reynolds stresses can be expressed as a function of the stream function:

$$\langle U'V'\rangle(Y) = -\mathrm{i}\eta(\tilde{\Psi}\partial_Y\tilde{\Psi}^* - \tilde{\Psi}^*\partial_Y\tilde{\Psi}). \tag{B26}$$

If we neglect the meridional derivative of the prefactor $(M_0(Y))^{-1/2} = (L_u^{1/2}(Y)(1 - B(Y))^{1/2})^{-1/2}$, consistent with the assumption of a slowly varying zonal flow, then we obtain the simple WKB expression

$$\begin{aligned}
\langle U'V'\rangle(Y) &= \pm F_0M_0(0)\exp\left(\pm\int_0^Y L_u(Y')^{3/2}(1 - B(Y'))^{1/2}dY'\right), \\
&= \pm F_0\left(\frac{1 - \gamma^{-1}\partial_{Y'}^2\langle U\rangle_{Y=0}}{(\langle U\rangle_{Y=0} + 1)}\right)^{1/2} \exp\left(\pm\int_0^Y \frac{\left(1 - \gamma^{-1}\partial_{Y'}^2\langle U\rangle\right)^{1/2}}{(\langle U\rangle + 1)^{3/2}}dY'\right),
\end{aligned} \tag{B27}$$

where F_0 is a positive constant. We note that since the zonal flow is allowed to take nonzero values at the forcing location ($Y = 0$), the dependence in $\langle U\rangle_{Y=0}$ is recovered in the expression of the

Reynolds stresses. This has already been noted in the Holten-Lindzen-Plumb model in the case of free-slip boundary condition (see Eq. (57) in Renaud and Venaille [26]).

This mathematical derivation shows that for the solution to be consistent with the WKB approximation, we are, in theory, restricted to explore cases where

(1) $\gamma \gg 1$,
(2) $(\langle U\rangle + 1)^{-1}\gamma^{-1/2} \ll 1$,
(3) $\frac{\partial}{\partial Y}(\frac{1-\gamma^{-1}\partial_Y^2\langle U\rangle}{\langle U\rangle+1})^{-1/4} \ll 1$, consistent with the assumption of a slowly varying wave amplitude, and hence slowly varying zonal flow,

and we should verify a posteriori that the term $\gamma^{-1}\frac{\partial^2\langle U\rangle}{\partial Y^2}$ is of order 1.

For completeness, we provide the WKB expression of the Reynolds stresses in its dimensional form:

$$\langle u'v'\rangle(y) = \pm F_0 c^2\left(\frac{1-\beta^{-1}\partial_y^2\langle u\rangle_0}{\langle u\rangle_0/|c|+1}\right)^{1/2}\exp\left(\pm\frac{1}{\Lambda}\int_0^y\frac{\left[1-\beta^{-1}\partial_{y'}^2\langle u\rangle\right]^{1/2}}{[\langle u\rangle/|c|+1]^{3/2}}dy'\right). \tag{B28}$$

The integrand is the inverse of an attenuation length. In the absence of zonal flow, this length is simply Λ. In the presence of a zonal flow, the attenuation is modified by the feedback of the zonal flow on the waves. Equation (B28) thus describes how Rossby waves deposit their momentum as they are attenuated, taking into account that they can be more or less attenuated depending on the zonal flow velocity and curvature. Since the WKB expression for the Reynolds stresses (B27) only depends on the zonal flow velocity and curvature, it provides a way of closing the problem and we can now directly solve for the one-dimensional zonal flow evolution equation (32), which becomes an integrodifferential equation for $\langle U\rangle$.

3. Prograde acceleration in the forcing region

For a single latitude of emission Y_0, we need to consider two waves, one propagating poleward ($Y > Y_0$), and the other propagating southward ($Y < Y_0$), The Reynolds stresses divergence is therefore the sum of the contribution of the northward wave ($\langle U'V'\rangle^+_{\mathrm{WKB}}$), the southward wave ($\langle U'V'\rangle^-_{\mathrm{WKB}}$), and the Reynolds stresses divergence at the forcing latitude ($\langle U'V'\rangle_F$):

$$-\frac{\partial}{\partial Y}\langle U'V'\rangle = -\frac{\partial}{\partial Y}\langle U'V'\rangle^+_{\mathrm{WKB}} - \frac{\partial}{\partial Y}\langle U'V'\rangle^-_{\mathrm{WKB}} - \frac{\partial}{\partial Y}\langle U'V'\rangle_F, \tag{B29}$$

where

$$-\frac{\partial}{\partial Y}\langle U'V'\rangle^+_{\mathrm{WKB}} = -F_0 M_0(Y_0)G(U)\exp\left(-\int_{Y_0}^{Y} G(U(Y'))dY'\right) \quad \text{for } Y > Y_0, \tag{B30}$$

$$-\frac{\partial}{\partial Y}\langle U'V'\rangle^-_{\mathrm{WKB}} = -F_0 M_0(Y_0)G(U)\exp\left(+\int_{Y_0}^{Y} G(U(Y'))dY'\right) \quad \text{for } Y < Y_0, \tag{B31}$$

where the integrand represents the inverse of a dimensionless attenuation distance

$$G(U(Y,T)) = \frac{\left(1-\gamma^{-1}\partial_Y^2\langle U\rangle\right)^{1/2}}{(\langle U\rangle+1)^{3/2}}, \tag{B32}$$

and

$$M_0(Y_0) = \left(\frac{1-\gamma^{-1}\partial_Y^2\langle U\rangle_{Y=Y_0}}{(\langle U\rangle_{Y=Y_0}+1)}\right)^{1/2}. \tag{B33}$$

The Reynolds stresses, $\langle U'V'\rangle$, do a jump of $-2F_0M_0(Y_0)$ at the forcing latitude, Y_0 (see Fig. 1(b)). The Reynolds stresses divergence would then be $2F_0M_0(Y_0)\delta(Y-Y_0)$ where δ is the Dirac distribution. This is nonphysical and would correspond to an infinite prograde acceleration of the zonal flow at $Y = Y_0$. We regularize this prograde acceleration over a Gaussian of finite width, ΔY, such that its integral over the domain is $2F_0M_0(Y_0)$:

$$-\frac{\partial}{\partial Y}\langle U'V'\rangle_F = \frac{2F_0M_0(Y_0)}{\sqrt{\pi}\,\Delta Y}\exp\left(-\left(\frac{Y-Y_0}{\Delta Y}\right)^2\right). \tag{B34}$$

Doing so, we introduce a new free parameter, ΔY, representing the width of the forcing region.

APPENDIX C: COALESCENCE CONTROLLED BY THE WIDTH OF THE FORCING REGION

Figure 16 illustrates the coalescence process when the limiting factor is the width of the forcing region.

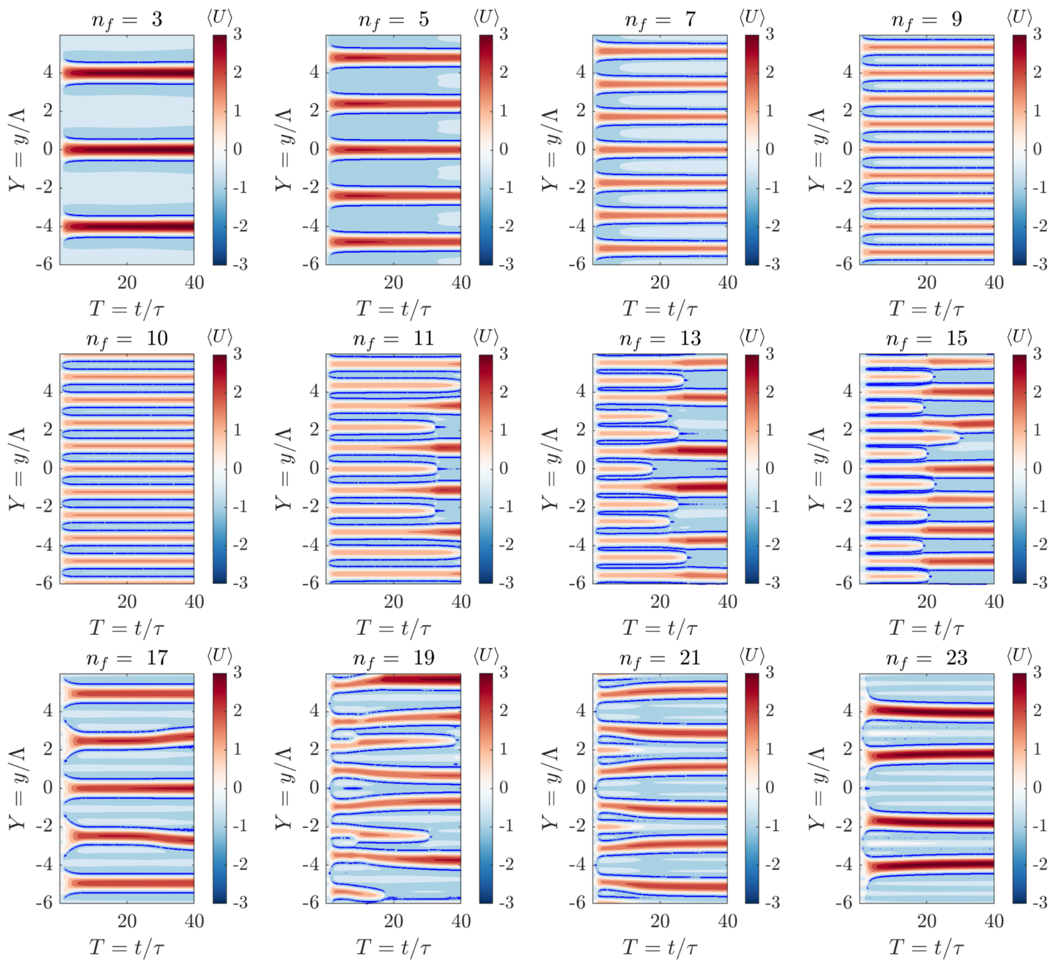

FIG. 16. Parameter sweep with decreasing initial jet spacing ($\gamma = 100$, Re $= 100$, $\Delta Y = 0.5$). The number of forcing latitudes, n_f is indicated at the top of each panel. The initial jet spacing is $D_{\text{jet,i}} = 12/n_f$ and goes from 12 to 0.52. Blues lines indicate critical latitudes ($-1 < \langle U \rangle < -0.99$).

[1] B. Galperin and P. L. Read, *Zonal Jets: Phenomenology, Genesis, and Physics* (Cambridge University Press, Cambridge, UK, 2019).
[2] C. Guervilly and P. Cardin, Multiple zonal jets and convective heat transport barriers in a quasi-geostrophic model of planetary cores, Geophys. J. Int. **211**, 455 (2017).
[3] A. P. Showman, X. Tan, and V. Parmentier, Atmospheric dynamics of hot giant planets and brown dwarfs, Space Sci. Rev. **216**, 139 (2020).
[4] J. Marston and S. Tobias, Recent developments in theories of inhomogeneous and anisotropic turbulence, Annu. Rev. Fluid Mech. **55**, 351 (2023).
[5] F. Bouchet, C. Nardini, and T. Tangarife, Kinetic theory of jet dynamics in the stochastic barotropic and 2D Navier-Stokes equations, J. Stat. Phys. **153**, 572 (2013).
[6] J. Marston, E. Conover, and T. Schneider, Statistics of an unstable barotropic jet from a cumulant expansion, J. Atmos. Sci. **65**, 1955 (2008).
[7] S. Tobias, K. Dagon, and J. Marston, Astrophysical fluid dynamics via direct statistical simulation, Astrophys. J. **727**, 127 (2011).
[8] B. F. Farrell and P. J. Ioannou, Structural stability of turbulent jets, J. Atmos. Sci. **60**, 2101 (2003).
[9] B. F. Farrell and P. J. Ioannou, Structure and spacing of jets in barotropic turbulence, J. Atmos. Sci. **64**, 3652 (2007).
[10] N. C. Constantinou, B. F. Farrell, and P. J. Ioannou, Emergence and equilibration of jets in beta-plane turbulence: Applications of stochastic structural stability theory, J. Atmos. Sci. **71**, 1818 (2014).
[11] N. C. Constantinou, Formation of large-scale structures by turbulence in rotating planets, Ph.D. thesis, arXiv:1503.07644.
[12] K. Srinivasan and W. Young, Reynolds stress and eddy diffusivity of β-plane shear flows, J. Atmos. Sci. **71**, 2169 (2014).
[13] W. Jackman and J. Esler, Parameterisation of small-scale random forcing in β-plane turbulence, J. Fluid Mech. **962**, A5 (2023).
[14] E. Woillez and F. Bouchet, Barotropic theory for the velocity profile of Jupiter's turbulent jets: An example for an exact turbulent closure, J. Fluid Mech. **860**, 577 (2019).
[15] J. Laurie, G. Boffetta, G. Falkovich, I. Kolokolov, and V. Lebedev, Universal profile of the vortex condensate in two-dimensional turbulence, Phys. Rev. Lett. **113**, 254503 (2014).
[16] A. Frishman, The culmination of an inverse cascade: Mean flow and fluctuations, Phys. Fluids **29**, 125102 (2017).
[17] A. Frishman and C. Herbert, Turbulence statistics in a two-dimensional vortex condensate, Phys. Rev. Lett. **120**, 204505 (2018).
[18] D. Andrews and M. E. Mcintyre, Planetary waves in horizontal and vertical shear: The generalized Eliassen-Palm relation and the mean zonal acceleration, J. Atmos. Sci. **33**, 2031 (1976).
[19] R. A. Plumb, The interaction of two internal waves with the mean flow: Implications for the theory of the quasi-biennial oscillation, J. Atmos. Sci. **34**, 1847 (1977).
[20] R. A. Plumb and A. D. McEwan, The instability of a forced standing wave in a viscous stratified fluid: A laboratory analogue of the quasi-biennial oscillation, J. Atmos. Sci. **35**, 1827 (1978).
[21] A. D. McEwan, R. O. R. Y. Thompson, and R. A. Plumb, Mean flows driven by weak eddies in rotating systems, J. Fluid Mech. **99**, 655 (1980).
[22] B. Semin, G. Facchini, F. Pétrélis, and S. Fauve, Generation of a mean flow by an internal wave, Phys. Fluids **28**, 096601 (2016).
[23] B. Semin, N. Garroum, F. Pétrélis, and S. Fauve, Nonlinear saturation of the large scale flow in a laboratory model of the quasibiennial oscillation, Phys. Rev. Lett. **121**, 134502 (2018).
[24] S. J. Lighthill, Acoustic streaming, J. Sound Vib. **61**, 391 (1978).
[25] G. K. Vallis, *Atmospheric and Oceanic Fluid Dynamics: Fundamentals and Large-scale Circulation*, 2nd ed. (Cambridge University Press, Cambridge, UK, 2017).
[26] A. Renaud and A. Venaille, On the Holton–Lindzen–Plumb model for mean flow reversals in stratified fluids, Quart. J. Roy. Meteorol. Soc. **146**, 2981 (2020).
[27] D. Lemasquerier, B. Favier, and M. Le Bars, Zonal jets at the laboratory scale: Hysteresis and Rossby waves resonance, J. Fluid Mech. **910**, A18 (2021).

[28] D. Lemasquerier, Experimental and numerical study of Jupiter's dynamics: Jets, vortices and zonostrophic turbulence, Ph.D. thesis, Aix-Marseille Université, 2021.

[29] T. Warn and H. Warn, On the development of a Rossby wave critical level, J. Atmos. Sci. **33**, 2021 (1976).

[30] K. Stewartson, The evolution of the critical layer of a Rossby wave, Geophys. Astrophys. Fluid Dynam. **9**, 185 (1977).

[31] L. Campbell, Wave–mean-flow interactions in a forced Rossby wave packet critical layer, Stud. Appl. Math. **112**, 39 (2004).

[32] L. J. Campbell, Wave-mean-flow interactions in atmospheric fluid flows, Notices Amer. Math. Soc. **70**, 1 (2023).

[33] N. C. Constantinou, G. L. Wagner, L. Siegelman, B. C. Pearson, and A. Palóczy, Geophysicalflows.Jl: Solvers for geophysical fluid dynamics problems in periodic domains on CPUs & GPUs, J. Open Source Softw. **6**, 3053 (2021).

[34] B. Galperin, S. Sukoriansky, and N. Dikovskaya, Zonostrophic turbulence, Phys. Scr. **T132**, 014034 (2008).

[35] S. M. Tobias and J. B. Marston, Direct statistical simulation of out-of-equilibrium jets, Phys. Rev. Lett. **110**, 104502 (2013).

[36] P. C. Cornillon, E. Firing, A. F. Thompson, L. M. Ivanov, I. Kamenkovich, C. E. Buckingham, and Y. D. Afanasyev, Oceans, in *Zonal Jets: Phenomenology, Genesis, and Physics*, edited by B. Galperin and P. L. Read (Cambridge University Press, Cambridge, UK, 2019), pp. 46–71.

[37] J. L. Mitchell, T. Birner, G. Lapeyre, N. Nakamura, P. L. Read, G. Riviére, A. Sánchez-Lavega, and G. K. Vallis, Terrestrial atmospheres, in *Zonal Jets: Phenomenology, Genesis, and Physics*, edited by B. Galperin and P. L. Read (Cambridge University Press, Cambridge, UK, 2019), pp. 9–45.

[38] Y. Afanasyev, S. O'leary, P. B. Rhines, and E. Lindahl, On the origin of jets in the ocean, Geophys. Astrophys. Fluid Dynam. **106**, 113 (2012).

[39] J. L. Mitchell and G. K. Vallis, The transition to superrotation in terrestrial atmospheres, J. Geophys. Res.: Planets **115**, E12 (2010).

[40] S. F. Potter, G. K. Vallis, and J. L. Mitchell, Spontaneous superrotation and the role of Kelvin waves in an idealized dry GCM, J. Atmos. Sci. **71**, 596 (2014).

[41] J. Liu and T. Schneider, Mechanisms of jet formation on the giant planets, J. Atmos. Sci. **67**, 3652 (2010).

[42] A. P. Showman and L. M. Polvani, Equatorial superrotation on tidally locked exoplanets, Astrophys. J. **738**, 71 (2011).

[43] M. Allison, Planetary waves in Jupiter's equatorial atmosphere, Icarus **83**, 282 (1990).

[44] J. Arregi, J. Rojas, A. Sánchez-Lavega, and A. Morgado, Phase dispersion relation of the 5-micron hot spot wave from a long-term study of Jupiter in the visible, J. Geophys. Res.: Planets **111**, E9 (2006).

[45] L. Li, A. P. Ingersoll, A. R. Vasavada, A. A. Simon-Miller, R. K. Achterberg, S. P. Ewald, U. A. Dyudina, C. C. Porco, R. A. West, and F. M. Flasar, Waves in Jupiter's atmosphere observed by the Cassini ISS and CIRS instruments, Icarus **185**, 416 (2006).

[46] G. S. Orton, A. J. Friedson, P. A. Yanamandra-Fisher, J. Caldwell, H. B. Hammel, K. H. Baines, J. T. Bergstralh, T. Z. Martin, R. A. West, G. J. Veeder Jr *et al.*, Spatial organization and time dependence of Jupiter's tropospheric temperatures, 1980–1993, Science **265**, 625 (1994).

[47] A. A. Simon-Miller, D. Banfield, and P. J. Gierasch, An HST study of Jovian chromophores, Icarus **149**, 94 (2001).

[48] B. M. Fisher, G. S. Orton, J. Liu, T. Schneider, M. E. Ressler, and W. F. Hoffman, The organization of Jupiter's upper tropospheric temperature structure and its evolution, 1996–1997, Icarus **280**, 268 (2016).

[49] L. Fletcher, G. Orton, J. Sinclair, P. Donnelly, H. Melin, J. Rogers, T. Greathouse, Y. Kasaba, T. Fujiyoshi, T. Sato *et al.*, Jupiter's north equatorial belt expansion and thermal wave activity ahead of Juno's arrival, Geophys. Res. Lett. **44**, 7140 (2017).

[50] J. L. Gunnarson, K. M. Sayanagi, J. J. Blalock, L. N. Fletcher, A. P. Ingersoll, U. A. Dyudina, S. P. Ewald, and R. L. Draham, Saturn's new ribbons: Cassini observations of planetary waves in Saturn's 42N atmospheric jet, Geophys. Res. Lett. **45**, 7399 (2018).
[51] C. C. Porco, R. A. West, A. McEwen, A. D. Del Genio, A. P. Ingersoll, P. Thomas, S. Squyres, L. Dones, C. D. Murray, T. V. Johnson *et al.*, Cassini imaging of Jupiter's atmosphere, satellites, and rings, Science **299**, 1541 (2003).
[52] C. Li, T. Le, X. Zhang, and Y. L. Yung, A high-performance atmospheric radiation package: With applications to the radiative energy budgets of giant planets, J. Quant. Spectrosc. Radiat. Transfer **217**, 353 (2018).
[53] C. Salyk, A. P. Ingersoll, J. Lorre, A. Vasavada, and A. D. Del Genio, Interaction between eddies and mean flow in Jupiter's atmosphere: Analysis of cassini imaging data, Icarus **185**, 430 (2006).
[54] A. Klocker and D. P. Marshall, Advection of baroclinic eddies by depth mean flow, Geophys. Res. Lett. **41**, 3517 (2014).
[55] J. Tollefson, M. H. Wong, I. de Pater, A. A. Simon, G. S. Orton, J. H. Rogers, S. K. Atreya, R. G. Cosentino, W. Januszewski, R. Morales-Juberías *et al.*, Changes in Jupiter's zonal wind profile preceding and during the Juno mission, Icarus **296**, 163 (2017).
[56] E. García-Melendo, S. Pérez-Hoyos, A. Sánchez-Lavega, and R. Hueso, Saturn's zonal wind profile in 2004–2009 from Cassini ISS images and its long-term variability, Icarus **215**, 62 (2011).
[57] E. van Sebille, I. Kamenkovich, and J. K. Willis, Quasi-zonal jets in 3-D Argo data of the northeast Atlantic, Geophys. Res. Lett. **38**, L02606 (2011).
[58] B. Galperin, S. Sukoriansky, R. M. B. Young, R. Chemke, Y. Kaspi, P. L. Read, and N. Dikovskaya, Barotropic and zonostrophic turbulence, in *Zonal Jets: Phenomenology, Genesis, and Physics*, edited by B. Galperin and P. L. Read (Cambridge University Press, Cambridge, UK, 2019), pp. 220–237.
[59] P. Léard, D. Lecoanet, and M. Le Bars, Multimodal excitation to model the quasibiennial oscillation, Phys. Rev. Lett. **125**, 234501 (2020).
[60] D. Lemasquerier, Dataset for "Emergence and coalescence of zonal jets: A quasilinear Rossby wave-mean flow interaction model", Zenodo (2025), https://doi.org/10.5281/zenodo.17550090.